20. Filgueira, L. Fluorescence-based staining for tartrate-resistant acidic phosphatase (TRAP) in osteoclasts combined with other fluorescent dyes and protocols. *J. Histochem. Cytochem.* 52, 411–414 (2004).
21. Stoller, P., Reiser, K. M., Celliers, P. M. & Rubenchik, A. M. Polarization-modulated second harmonic generation in collagen. *Biophys. J.* 82, 3330–3342 (2002).
22. Yu, X., Huang, Y., Collin-Osdoby, P. & Osdoby, P. Stromal cell-derived factor-1 (SDF-1) recruits osteoclast precursors by inducing chemotaxis, matrix metalloprotease-9 (MMP-9) activity, and collagen transmigration. *J. Bone Miner. Res.* 18, 1404–1418 (2003).
23. Katayama, Y. *et al.* Signals from the sympathetic nervous system regulate hematopoietic stem cell egress from bone marrow. *Cell* 124, 407–421 (2006).
24. Matloubian, M. *et al.* Lymphocyte egress from thymus and peripheral lymphoid organs is dependent on S1P receptor 1. *Nature* 427, 355–360 (2004).
25. Cyster, J. G. Chemokines, sphingosine-1-phosphate, and cell migration in secondary lymphoid organs. *Annu. Rev. Immunol.* 23, 127–159 (2005).
26. Kappos, L. *et al.* Oral fingolimod (FTY720) for relapsing multiple sclerosis. *N. Engl. J. Med.* 355, 1124–1140 (2006).
27. Tedesco-Silva, H. *et al.* FTY720 versus mycophenolate mofetil in de novo renal transplantation: six-month results of a double-blind study. *Transplantation* 84, 885–892 (2007).
28. Kobayashi, K. *et al.* Tumor necrosis factor α stimulates osteoclast differentiation by a mechanism independent of the ODF/RANKL-RANK interaction. *J. Exp. Med.* 191, 275–286 (2000).
29. Ishii, M. *et al.* RANKL-induced expression of tetraspanin CD9 in lipid raft membrane microdomain is essential for cell fusion during osteoclastogenesis. *J. Bone Miner. Res.* 21, 965–976 (2006).
30. Okamoto, H. *et al.* Inhibitory regulation of Rac activation, membrane ruffling, and cell migration by the G protein-coupled sphingosine-1-phosphate receptor EDG5 but not EDG1 or EDG3. *Mol. Cell. Biol.* 20, 9247–9261 (2000).

Supplementary Information is linked to the online version of the paper at www.nature.com/nature.

Acknowledgements We thank U. H. von Andrian and I. B. Mazo for their help with the technique of intravital skull bone imaging. We also thank Y. Takuwa and N. Sugimoto for discussions, and P. M. Murphy and S.Venkatesan for their help in imaging *in vitro* chemotaxis using the EZ-Taxiscan. This work was supported in part by the Intramural Research Program of the National Institute of Allergy and Infectious Diseases, NIH, US Department of Health and Human Services, and by a fellowship grant to M.I. from the International Human Frontier Science Program.

Author Contributions M.I. performed most of experiments, with the assistance of J.G.E. and Y.S. for two-photon microscopy and for the *in vitro* osteoclast culture system, respectively. F.K. developed the unsupervised segmentation software and performed the computational analyses used to quantify the osteoclast-bone surface interface, with the assistance of M.M.-S. J.V. and R.L.P. generated *CD11b-Cre* transgenic and *S1PR1*^{loxP} knock-in mice, respectively. R.N.G. helped M.I. in designing and interpreting experiments, as well as in writing the paper.

Author Information Reprints and permissions information is available at www.nature.com/reprints. Correspondence and requests for materials should be addressed to R.N.G. (rgermain@niaid.nih.gov).

METHODS

Cell culture. The RAW264.7 cell line and mouse BM-MDM cells, which contain osteoclast precursor cells, were cultured as previously described[28,29]. To stimulate osteoclastogenesis, 50 ng ml^{-1} RANKL (PeproTech) was added to the medium and the cells were incubated for 3 to 4 days.

Conventional and quantitative RT–PCR amplification. Conventional RT–PCR was performed as described previously[29]. Primers used are listed in Supplementary Table 4. Relative quantification with real-time RT–PCR was performed using an ABI PRISM 7900 (Applied Biosystems Inc.) with an Assay-on Demand TaqMan probe and relevant primers, according to the manufacturer's instructions.

Determination of Rac activity. Pulldown assay methods to determine the GTP-bound active form of Rac have been described in detail previously[30].

***In vitro* chemotaxis chamber assay.** Chemotactic migration of cells was measured in a modified Boyden chamber as described previously[27].

EZ-Taxiscan chemotaxis assay. Chemotaxis experiments were also conducted in an EZ-Taxiscan chamber according to the manufacturer's protocol (Effector Cell Institute). The EZ-Taxiscan is a visually-accessible chemotactic chamber, in which one compartment containing ligand (S1P) and another compartment containing cells are connected by a microchannel. Phase contrast images of migrating cells were acquired at 1 min intervals.

Mice. C57BL/6 mice, CX_3CR1–EGFP knock-in mice[12], CSF1R (M-CSF receptor)–EGFP transgenic mice[14], were obtained from The Jackson Laboratory. The generation of the loxP-flanked *S1PR1* allele (*S1PR1*^{loxP})[18] and osteoclast/monocyte lineage-specific *CD11b-Cre* transgenic mice[19] were described previously. *S1PR1*$^{-/+}$ × *CD11b-Cre* and *S1PR1*$^{loxP/+}$ × *CD11b-Cre* littermates were born at expected frequencies and were viable and fertile, but live *S1PR1*$^{loxP/loxP}$ × *CD11b-Cre* littermates were obtained rarely (three viable *S1PR1*$^{loxP/loxP}$ × *CD11b-Cre* out of 59 total mice), suggesting possible embryonic lethality as seen with global $S1P_1$ deficiency. All mice were bred and maintained under specific pathogen-free conditions at animal facilities of NIH. Mutant mice were genotyped by PCR[18,19]. All mice were housed and handled according to NIH institutional guidelines under an approved protocol.

Immunohistochemistry. Immunohistological analyses were performed as described previously[2]. Anti-mouse $S1P_1$ rabbit polyclonal antibody was purchased from Affinity Bioreagents. In some experiments, fluorescence-based staining for TRAP[20] with ELF 97 substrate (Molecular Probes) was used with some modifications.

Two-photon intravital bone tissue imaging. Intravital microscopy of mouse calvaria bone tissues was performed using a protocol modified from a previous report[10,11]. Mice were anaesthetized with isoflurane (Baxter, 2.5% vaporized in an 80:20 mixture of oxygen and air), and the hair in the neck and scalp was removed with hair removal lotion (Nair). The frontoparietal skull was exposed and the mouse head was immobilized in a custom-made stereotactic holder. A catheter was placed into the tail vein with a 30-gauge needle attached to PE-10 tubing (Becton Dickinson). The imaging system was composed of an LSM510 NLO multiphoton microscope (Carl Zeiss) driven by a Chameleon XR Ti:Sapphire laser (Coherent) tuned to 880 nm, and an inverted microscope (Axiovert 200; Carl Zeiss) equipped with a ×40 water immersion objective (Achroplan IR, NA 0.8; Carl Zeiss). Fluorescent cells were detected through a bandpass emission filter at 525/50 nm (for EGFP). Vessels were visualized by injecting 70 kDa Texas Red conjugated-dextran (detected using a 620/60 nm filter) intravenously immediately before imaging. Image stacks were collected at 3-μm vertical step size at a depth of 100–150 μm below the skull bone surface. For three-dimensional videos, four sequential image stacks were acquired at 3 μm z spacing to cover a volume of 154 × 154 × 9.0 μm. The time resolution was 1 min. Raw imaging data were processed with Imaris (Bitplane) with a Gaussian filter for noise reduction.

Ovariectomy and FTY720 treatment. Twelve 12-week-old female, ovariectomized or sham-operated, C57BL/6J mice were purchased from Charles River Laboratories. Mice were injected intraperitoneally either with FTY720 (3 mg kg^{-1}, Cayman Chemical) dissolved in a vehicle (PBS containing 5% acidified DMSO and 30% fatty acid-free BSA) or with vehicle only, daily for 4 weeks. The mice were then killed and femurs were excised and fixed. Uteri of all the animals were excised and were weighed to evaluate the effect of ovariectomy.

Bone histomorphometry. Trabecular bone morphometry within the metaphyseal region of distal femur was quantified using micro-CT (μCT40, Scanco Medical AG). Volumeric regions for trabecular analysis were selected within the endosteal borders to include the central 80% of vertebral height and secondary spongiosa of femoral metaphyses located ~6% of the total length from the growth plate. Trabecular morphometry was characterized by measuring the bone volume fraction (bone volume/total volume), trabecular thickness and trabecular number. To assess the attachment of osteoclasts to the bone surface, osteoclasts and bone trabeculae were fluorescently visualized in sections by two-photon microscopy. To identify osteoclasts, fluorescence based TRAP staining[20] was performed. Collagen-enriched bone matrices could be visualized using the second harmonic emission from collagen fibres excited by infrared lasers. Sections were examined using a two-photon laser microscope (laser was tuned to 780 nm). Fluorescence was detected through bandpass emission filters at 370–450 nm (for second harmonic emission from bone matrices) or 525/50 nm (for TRAP staining). Image analysis was performed using a fully automated segmentation approach (no manual tracing of cell/tissue boundaries or other user intervention required) and the 'osteoclast attachment ratio' was calculated as the ratio 'bone surface attached by osteoclasts/total bone surface' (F.K., submitted manuscript).

Flow cytometry. All reagents were purchased from BD PharMingen. To examine the composition of PMCs, blood was collected from the retro-orbital plexus with a heparinized glass pipette, from mice treated intraperitoneally 4 h previously with FTY720 (3 mg kg^{-1}) or vehicle (Fig. 4), or treated intravenously 1 h previously with SEW2871 (5 mg kg^{-1}) or vehicle (Supplementary Fig. 4). After removing the red blood cells using ACK lysis buffer (Invitrogen), cells were stained with Alexa647-conjugated anti-F4/80 (Fig. 4), or FITC-conjugated anti-CD11b and PE-Cy7-conjugated anti-CD3 (Supplementary Figs 4 and 9), using conventional methods. Flow cytometric data were collected on a FACSCalibur (Becton Dickinson) and analysed with FlowJo software (TreeStar).

Quantifying cellular interaction dynamics in 3D fluorescence microscopy data

Frederick Klauschen[1,2], Masaru Ishii[3,4], Hai Qi[3], Marc Bajénoff[3,4], Jackson G Egen[3], Ronald N Germain[1,3] & Martin Meier-Schellersheim[1]

[1]Program in Systems Immunology and Infectious Disease Modeling, National Institute of Allergy and Infectious Diseases, National Institutes of Health, Bethesda, Maryland, USA. [2]Institute of Pathology, Universitätsmedizin Berlin, Berlin, Germany. [3]Lymphocyte Biology Section, Laboratory of Immunology, National Institute of Allergy and Infectious Diseases, National Institutes of Health, Bethesda, Maryland, USA. [4]Present addresses: Laboratory of Biological Imaging, Immunology Frontier Research Center (IFReC), Osaka University, 3-1 Yamada-oka, Suita 565-0871, Japan (M.I.), INSERM U924, Institut de Pharmacologie Moleculaire et Cellulaire, Centre National de la Recherche Scientifique, Université de Nice-Sophia-Antipolis, Valbonne, France (M.B.). Correspondence should be addressed to F.K. (fklauschen@mail.nih.gov) or M.M.-S. (mms@niaid.nih.gov).

Published online 20 August 2009; doi:10.1038/nprot.2009.129

The wealth of information available from advanced fluorescence imaging techniques used to analyze biological processes with high spatial and temporal resolution calls for high-throughput image analysis methods. Here, we describe a fully automated approach to analyzing cellular interaction behavior in 3D fluorescence microscopy images. As example application, we present the analysis of drug-induced and $S1P_1$-knockout-related changes in bone–osteoclast interactions. Moreover, we apply our approach to images showing the spatial association of dendritic cells with the fibroblastic reticular cell network within lymph nodes and to microscopy data regarding T–B lymphocyte synapse formation. Such analyses that yield important information about the molecular mechanisms determining cellular interaction behavior would be very difficult to perform with approaches that rely on manual/semi-automated analyses. This protocol integrates adaptive threshold segmentation, object detection, adaptive color channel merging, and neighborhood analysis and permits rapid, standardized, quantitative analysis and comparison of the relevant features in large data sets.

INTRODUCTION

The availability and usage of advanced fluorescence imaging techniques such as confocal and multi-photon microscopy have dramatically increased and enabled researchers to investigate biological processes with a high degree of spatial and temporal resolution. This includes, but is not limited to, studies ranging from static detection of the subcellular localization of proteins to dynamic tracking of fluorescent probes in single cells to intravital imaging of cell behavior in complex tissues and organs. These developments have been especially fruitful in fields such as immunology, cancer research and neuroscience, where the system behavior is largely governed by dynamic cell interactions, for instance, by the interactions between lymphocytes and antigen-presenting cells in lymph nodes[1–3], lymphocyte recruitment to and interaction with tumors[4] and synapse–glia dynamics in the brain[5]. Quantitative analysis of cell interaction behavior can considerably increase the information we can gain about the molecular mechanisms governing cellular communication processes or may be used to assess and quantify the efficacy of drugs. However, the development of computational high-throughput methods for automated and standardized quantitative analysis of the resulting 3D image data has lagged behind the experimental advances[6].

Here, we describe a protocol for the quantitative investigation of cell–cell, cell–tissue or cell–pathogen interactions that uses a fully automated, high-throughput image analysis method. The approach involves four steps that are carried out automatically without user intervention: First, the actual (true-positive) signal is separated from background (false-positive image elements) in each fluorescent image channel. Second, individual image objects are detected in the output data of the first step, which permits acquiring object numbers and size statistics and allows for the removal of image artifacts based on prior information about, for instance, minimum cell size. The third step merges the different fluorescent color channels to obtain an unambiguous segmentation. This step is especially important for interaction analyses because interfacing objects of different types (i.e., different colors) usually show a spatial image overlap that an accurate interface analysis must account for. Finally, in the last step, the interface areas are computed.

Advantages and disadvantages of our method

Previous approaches to interaction image analysis relied on semi-quantitative estimations using manual measurements of such features. For example, in conventional bone–osteoclast interaction analysis, data sets are sent to commercial labs and processed by personnel who manually delineate cellular boundaries and interfaces[7–11]. In contrast, the method presented here enables investigators to carry out rapid and standardized analyses that do not require operator interpretation in the vast majority of cases and are especially suited to the quantification of differences between experimental groups in large 3D data sets.

To assess the limitations and the usability of our protocol for different data types and image features, we tested different types of typical confocal/two-photon image data (see details below) that are acquired by different experimenters using different microscopy platforms. Moreover, we carried out sensitivity analyses by assessing the impact of the variation of the threshold selection parameter and the introduction of artificial image noise on the interface analysis. These tests showed that our approach works equally well for all data types we tested and that parameter/quality variations did not significantly affect the interface analysis results. However, we tested *typical* image data and noise. A limitation of the protocol (and segmentation approaches in general) is that excessive noise and/or

high background signal (approaching the intensity of the object signal) may lead to a failure of the ability of the method to separate noise/background from actual signal, which subsequently generates incorrect interface quantification results. As a rule of thumb, the protocol can be applied to image data whose intensity histogram meets the shape characteristics we describe. In contrast, the quality of the analysis can be expected to deteriorate when, for instance, the peak in the lower intensity region of the histogram representing the background 'collapses' into the higher intensity 'signal' region. However, we would like to point out that the main application of our protocol is the comparison of different experimental groups (e.g., see the following section) and that for this purpose (small) segmentation errors are acceptable as long as they occur consistently, which is guaranteed by our approach.

Example applications

The software we use in this protocol was initially developed for quantifying osteoclast–bone interactions in order to analyze how a $S1P_1$ (sphingosine-1-phosphate) receptor knockout mutant and the immunomodulatory drug FTY720 (Fingolimod, an $S1P_1$ agonist) that affect a lipid phosphate chemosensing pathway alter osteoclast activity *in situ*, thereby affecting bone homoeostasis[12]. We present this as our main example application and then show the versatility of the approach by describing its application to two other types of data. In the second example, we show how our approach can be used to analyze image data to quantify the extent to which dendritic cells attach to the fibroblastic reticular cell (FRC) networks on which T lymphocytes migrate within lymph nodes. The last example shows the applicability of the protocol for the investigation of interaction phenomena on a smaller scale: We analyze image data from recently published experiments[13] elucidating the influence of a mouse T-cell signaling mutation in the gene encoding SAP (signaling lymphocyte activation molecule (SLAM)-associated protein, the cause of X-linked lymphoproliferative syndrome (XLP)) on cell membrane contacts of T and B lymphocytes (this SAP mutation is known to affect the development of humoral immunity by influencing the stability of interactions between these T and B cells).

All these examples have in common that their analysis requires a quantitative assessment of either the size and/or the spatial localization of interfaces between cells or spatial regions with certain properties relevant for the biological question at hand, but differ in terms of size and shape of the cells and tissue structures.

The applications show the advantages of using an automated and standardized analysis method to perform unbiased comparisons of data sets that are obtained under different experimental conditions. As illustrated by the images in **Figures 1** and **2**, background fluorescence and the overlap between different color channels can make manual segmentation a challenging and subjective task. Under such conditions, variations in background signal/noise levels

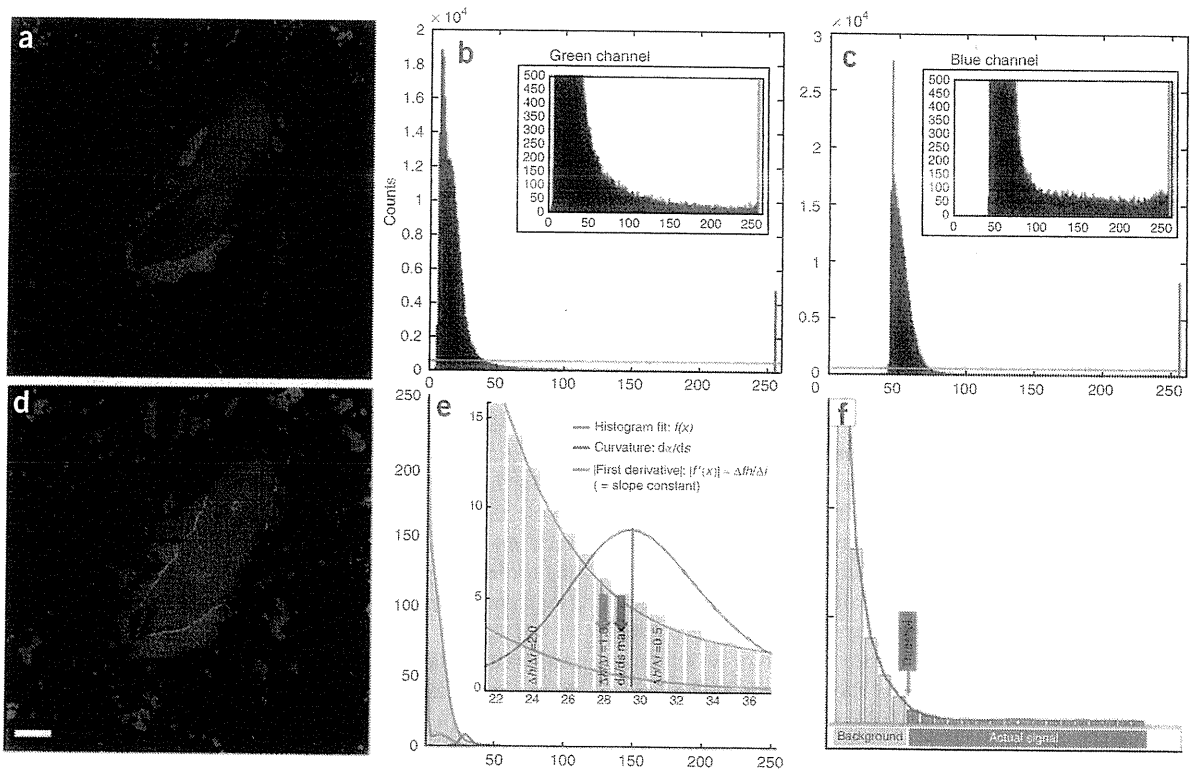

Figure 1 | Automated threshold segmentation. Example original (**a**) fluorescence two-photon image and intensity histograms showing the characteristic shape (**b**,**c**). Histograms can be divided into (1) a 'peak' region (lower intensity values) and (2) a 'constant' region stretching from the end of the 'peak' region to higher intensity values. (**b**) Osteoclasts (green) and (**c**) bone tissue (blue). (**d**) Resulting segmented image after automated thresholding using maximum curvature estimation method for threshold selection illustrated in panels **e** and **f**. (**e**) The curvature of the graph of the histogram fit (red) is shown in blue. Selection of the threshold at the curvature maximum is indicated by blue arrow. The approximation of the maximum curvature computation by the slope constant criterion $f'(x) \approx \Delta h/\Delta i = 1$ is depicted by the green curve and arrow. Scale bar = 10 μm. All animal procedures used in this study have been approved by the Animal Care and Use Committee, NIAID, NIH.

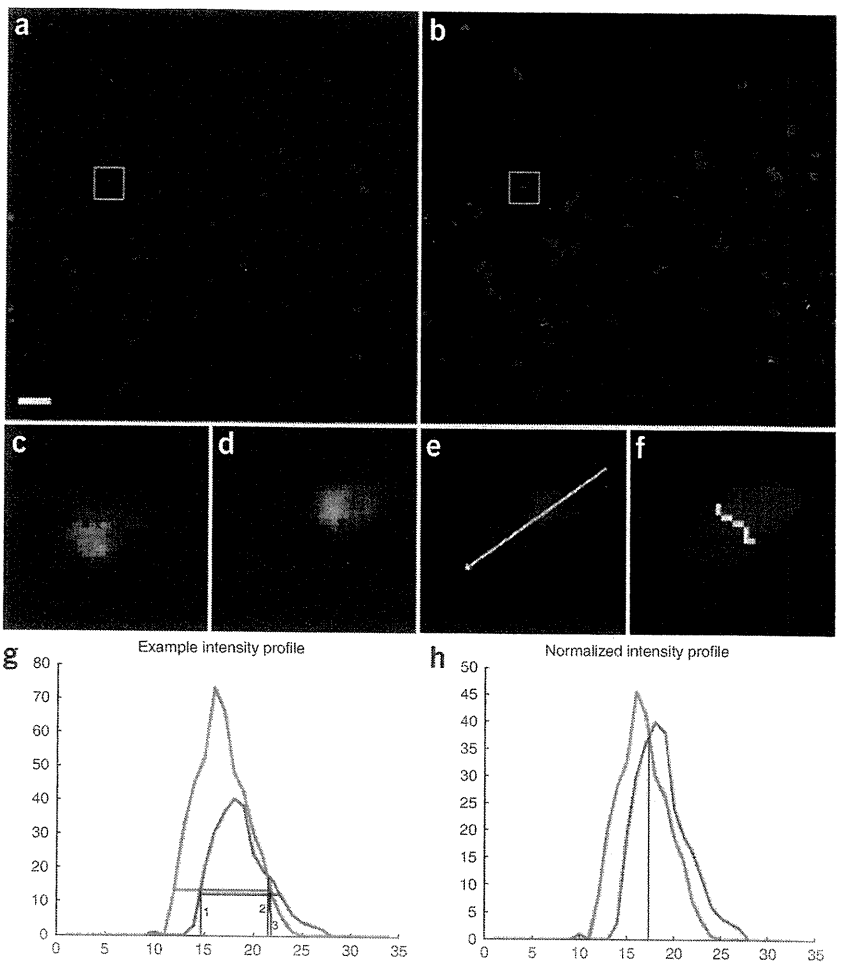

Figure 2 | Adaptive channel merging. (**a**) Original image data of T (green) and B (blue) cells. (**b**) Segmentation result, interacting T cells (red), interface (white). Magnification of blue (**c**) and green (**d**) channels with overlay (**e**) and segmentation result (**f**) from inset in panels **a** and **b**. Intensity profile along arrow in panel **e** is shown in panel **g**. Horizontal green and blue lines in panel **g** indicate computed threshold. Black vertical lines (1, 2 and 3) show the selection alternatives of the border between the blue and green channels under the condition that (1) either the blue or (3) the green object is given priority. Line 2 is the result of the border selection when comparing absolute intensities of competing channels. (**h**) Normalized intensity profile allows for balanced identification of the border between color channels (result shown in panel **f**). Scale bar = 10 μm. All animal procedures used in this study have been approved by the Animal Care and Use Committee, NIAID, NIH.

between data sets or between color channels in a single data set can easily mask subtle but significant biological differences or artificially create the impression of such differences. The potentially clinically relevant results obtained for the quantification of osteoclast–bone interaction robustly showed the ability of the immunomodulatory drug FTY720 to reduce the adhesion of osteoclasts to bone surfaces based on multiple data sets that display typical variations in image quality. This effect was not evident from visual inspection of the microscopy images and could be rigorously quantified only because of the adaptive standardization our protocol offers.

Detailed description of the image analysis program

The image analysis program performs the following steps automatically.

First module: Signal background separation by automated adaptive threshold segmentation. The critical step in image segmentation is the separation of signal from background, which includes discrimination of different signals (colors) from one another when considering multicolor fluorescence data sets. The first module of the image processing software that is used here performs an automated adaptive intensity threshold segmentation based on the characteristics of fluorescence confocal or two-photon image data. Such intensity histograms show a peak in the lower intensity region that represents the background signal, while the actual image signal is—relative to the form of the background part—approximately uniformly distributed over the (higher) intensity spectrum. We found this to be characteristic of all two-photon and confocal fluorescence microscopy images we analyzed and distinct from most conventional (non-fluorescent) image data (as in ref. 14) (**Fig. 1**). As the exact shape and location of the peak and a constant region vary depending on the image acquisition features, a stable and reliable segmentation method capable of yielding comparable results has to adapt to these variations that may occur between different as well as within individual data sets. The segmentation algorithm used here accomplishes this by defining the transition point between background and actual signal (i.e., the threshold), as the intensity value at which the curvature of the histogram graph is maximal (see 'Automatic adaptive thresholding: maximum curvature estimation' for details). In contrast to fully (3D) global thresholding methods with a single constant or user-selected cutoffs for the whole 3D image data set, our approach computes the threshold for each image *z*-slice separately and is therefore capable of compensating for intensity inhomogeneities (or 'attenuation') along the *z* axis (for instance, in deep-tissue two-photon imaging *in vivo*).

Automatic adaptive thresholding: maximum curvature estimation. In the case of photographic images, histograms often have a bimodal shape, with one peak representing background and the other signal portion of the image (**Supplementary Fig. 1**). In such cases, it is obvious that the threshold selection criterion is to find the minimum between the two peaks. There is no such criterion that is similarly obvious and also physically plausible in case of two-photon/confocal microscopy image data, and the transition between background and signal cannot be defined as a precise location similar to that in case of bimodal histograms. It can only be defined with some remaining degree of fuzziness in the region of

the transition between the strongly decaying part of the peak in the lower intensity spectrum and the region with the relatively flat slope. We chose the maximum curvature and its approximation using a derivative criterion for normalized histograms as threshold selection criterion, because it represents a mathematically definable, reasonable estimate of the transition point at which the strongly negative slope of the background peak changes to the relatively flat slope associated with the signal region and, moreover, because it is computationally efficient (alternative threshold selection criteria are discussed in ref. 14).

To compute the curvature of the (discrete) histogram in the relevant region, a Gaussian model may be used to fit the histogram in the relevant region, i.e., between global maximum (or local maximum with highest intensity value in the background region) and intensity 254. The maximum intensity histogram bin 255 is omitted in all calculations, because it is significantly higher than the other 'true positive' intensity values. This is due to the aggregation of all intensities ≥ 255 in this bin. We also omit the 0 bin, because in the case of image data of a low overall intensity (and thus many 0-intensity voxels) its inclusion may interfere with the generation of a normalized histogram that exhibits the shape features required for threshold computation.

Given the angle α, $f(x)$, the histogram fit function, and the line element ds, given by

$$ds = \sqrt{1 + (f'(x))^2}dx,$$

the curvature of the graph of $f(x)$ is given by

$$\frac{d\alpha}{ds} = \frac{d\alpha}{dx} \cdot \frac{dx}{ds} = \frac{f''(x)}{(1 + f'(x)^2)^{3/2}}$$

(**Fig. 1**). In our implementation, we used the discretized derivative of the histogram $h(i)$: To determine the intensity threshold used for the segmentation, the derivative $\Delta h/\Delta i$ is computed stepwise starting at $i=254$ with decreasing i until the transition from the constant image to the non-constant background region is encountered. Before determining the threshold, the histogram is smoothed using a Gaussian filter (0 bin is the maximum bin of intensity histogram) scaled by the histogram integral and multiplied by a factor of 255 in order to normalize for the different cell/bone tissue coverage of the image area. Owing to the common histogram shape features present in all data sets, this scaling/normalization procedure resulted in the value of the discrete derivative

$$\frac{\Delta h}{\Delta i} = \frac{h(i - \Delta i) - h(i)}{\Delta i}$$

to be ~ 1 at the maximum curvature point (**Fig. 1e**). Our sensitivity analysis of the precise location of the selected threshold (for details see 'Robustness assessment: Impact of variations of the slope constant on the interface area results') shows that this approximation is valid. **Supplementary Figure 2** shows an exemplary threshold segmentation result overlaid with the original image.

Second module: Object detection using connected component analysis. Following the automated thresholding procedure, our approach uses a 3D connected component labeling algorithm (see ref. 15 and references within) to identify individual image objects. The connected component labeling permits computation of the numbers of objects (such as cells) and the corresponding object features such as volume, surface area and location. It is also required for obtaining detailed information on cell–cell interaction behavior (e.g., the number of cells of type A attached to cells of type B) and for comparing features of potential interest of interacting versus non-interacting cells. In addition to the utility of the connected component analysis for the quantification of object features, our software also uses this analysis to improve image quality by applying a threshold filter for cell volumes, thus allowing removal from the processed data set of small pieces of cell debris or bright specks resulting from artifactual dye labeling.

Third and fourth modules: Channel merging and interface area computation using normalized intensity comparison and voxel-neighborhood analysis. The third step of the analysis pipeline finalizes the segmentation by adaptively merging the earlier separate segmentations of individual color channels. This is a pivotal step because most current image data involve objects (cells, pathogens and tissue components) that are labeled with different colors and whose fluorescent signals overlap when those objects are in close proximity, resulting in overlap in the segmentations of the individual color channels. Disregarding this issue may lead to distorted interaction results and even to the accidental removal of small objects, especially if one channel is significantly dimmer than the other. Our channel merging approach accounts for spatial overlap between neighboring or interacting image objects by combining the single-channel thresholding results with an adaptive intensity comparison of the original image data based on normalization of each channel with its intensity profile. After the initial threshold segmentation (carried out for each channel separately), each voxel that has been assigned both class labels ('overlap voxel') is evaluated by comparing the original image intensities in each channel normalized with the corresponding maximum intensity values. The voxel is then assigned to the final segmentation class that represents the channel with the higher relative intensity at that particular voxel. This approach therefore allows for an accurate estimate of the actual interfaces (see **Fig. 2** and **Supplementary Fig. 3**).

Finally, the interface areas are computed by identifying those voxels in channel 1 that are direct neighbors of voxels in channel 2. We use the sum of the surface voxels as an estimate of the total contact area. This is sufficient because the analysis result is provided in terms of ratios of interface areas to total cell or tissue surface areas or in terms of comparisons of such areas between different experimental groups.

Robustness assessment: impact of variations of the slope constant and noise on the interface area results. The robustness of an image segmentation and analysis method toward variations of pre-set parameters and image quality is an important measure of its utility. Therefore, we carried out a sensitivity analysis to evaluate the impact of variations in the slope value that is used to identify the boundary between background and true image data. This analysis showed that the average ratio of the interface area/total surface area in two groups (bone–osteoclast gene knockout versus wild-type data) with 20 data sets each (each data set consisting of ~ 10 x–y images of 512×512 pixels) changes only $\sim 10\%$ even when varying the slope value by a factor of 2 in both directions for both channels. More importantly, the differences of the average area ratios between the control and knockout groups—which is the relevant result in this kind of analysis—show a negligible dependence on the variation of the characteristic slope (change of

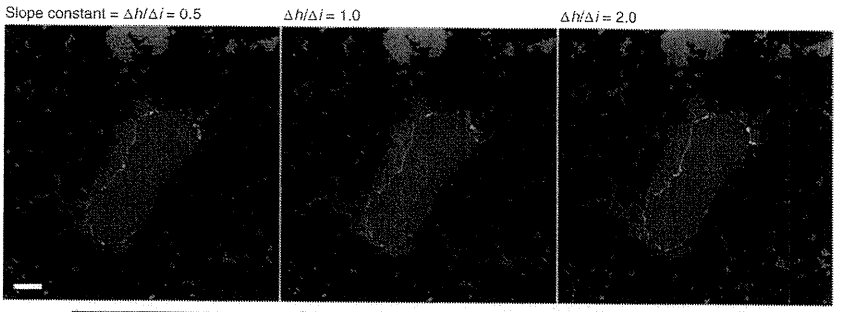

Figure 3 | Analysis of the impact of variations in the derivative constant on the normalized interface area (ratio of the interface area/total bone surface area) and on the difference between 'wild-type' and 'knockout' groups. Mean values are based on 20 data sets each in each group. Although changing the derivative constant by a factor of 2 in both directions relative to 1.0 results in average normalized interface area changes of ~10%, the differences change only 1.1% (0.5→1.0) and 2.2% (1.0→2.0). Scale bar = 10 μm. (For more information on the experiments see ref. 12.) All animal procedures used in this study have been approved by the Animal Care and Use Committee, NIAID, NIH.

	Normalized interface area (mean ± s.d.)		
Slope constant	0.5	1.0	2.0
Group 1 (wild type)	0.322 ± 0.151	0.369 ± 0.155	0.424 ± 0.157
Group 2 (knockout)	0.506 ± 0.181	0.551 ± 0.173	0.602 ± 0.162
Δ (group 1, 2)	0.184	0.182	0.178

difference is 1.1%; see **Fig. 3**). These results show that the particular choice of the slope value is less important than using the same constant throughout the data analysis, which subsequently generates the proper adaptive threshold value. This ensures that variations of image quality within and between data sets are normalized, thus permitting the consistent comparison of different data sets.

In addition to testing our approach with different types of typical confocal and two-photon microscopy data, we assessed the robustness of the analysis under the influence of various noise levels. We generated different levels of artificial noise for an exemplary data set (image noise follows a Poisson distribution[16]). The comparison of the analysis results yielded interface area differences of ≤5% between different typical Poisson noise levels (for details see **Supplementary Fig. 4**). However, because of the combination of noise and background signal and the diversity of possible features of fluorescence microscopy data, we cannot provide straightforward rules to determine a priori which data our protocol will work with. Low data quality may lead to significant misclassification (see **Supplementary Fig. 5**), and we therefore advise the user to carry out tests and examine test results to estimate the suitability of the automated analysis using this protocol and/or to optimize the user-definable parameters for the particular data. However, for the main application of this protocol, the comparative analysis of interaction behavior, it is above all important that data processing is standardized and that the data sets that are to be compared are of roughly similar quality. In that case, segmentation errors within reasonable limits are not problematic for comparative analyses using our protocol because they occur consistently.

MATERIALS

REAGENTS

Images for analysis, see REAGENT SETUP for further information about required format and **Supplementary Methods** for information on how images were acquired for our example applications.

EQUIPMENT

- Software (see EQUIPMENT SETUP for details)
- *Standard 32-bit hardware.* The example analyses shown in this protocol were performed on an Intel Xeon Dual Core 3.0 GHz workstation with 16 GB memory running 64-bit SuSE Linux. ▲ CRITICAL Although the analyses can in principle be performed on the standard 32-bit hardware, the memory requirements may go beyond 4 GB depending on image size and the number of biological objects in the image data, and 64-bit workstations with 8 GB or more memory may be required.

REAGENT SETUP

Image data preparation The analysis module of the software we present and use in this protocol requires image data to be in 3-color (RGB) Portable Network Graphics ('.png') format, with the *z*-slices in files consecutively numbered and assigned a defined filename prefix, for instance, 'img001.png, img002.png, img003.png ...'. Each *z*-stack has to be saved in a single directory that does not contain any entries other than the image files. If a 4D data set is analyzed, each time step is treated separately and saved in individual directories.

Note that because this protocol describes interactions between two types of biological objects, only two-color channels are relevant. Here, by convention, we use 'green' as the first and 'blue' as the second channel. Microscope acquisition software usually permits saving images in TIFF format files, with one file per color channel and slice (and in case of 4D data per time step) indicated by certain identifiers, for instance 'filenameprefix_T000_C0_Z000.tif,' where 'T', 'C' and 'Z' indicate time step, color channel and *z*-slice, respectively. The software '2PISA' offers a module to convert such data into the format described above, if this is not required the protocol should be started at Step 10.

Software The description of the analysis method we provide offers sufficient detail for its implementation with a suitable high-level scripting/programming language (e.g., MATLAB). However, we recommend using our implementation of the software '2PISA' (2-Photon Image Segmentation and Analysis), which can be obtained free of charge for non-commercial use from the authors (http://www3.niaid.nih.gov/labs/aboutlabs/psiim/computationalBiology/) and is available for most versions of Linux, Mac OS X and Windows. The software package is written in C/C++ using the Qt library. Although the current release of the software supports two-color images, the method can in principle handle an unlimited number of channels as long as each class has a unique color label. An OpenGL-capable system is required for full functionality.

PROCEDURE

Image data preparation

1| Start the program '2pisaloader' to prepare the data.

2| In the menu 'Data,' select 'Convert data.'

3| If the data one would like to convert is time course data, select 'yes' and enter the single character that identifies the nature of the image parameter of interest. If 'T' defines the time step identifier (which is followed by the time step number, for

instance 'T001' defines the first time step), enter 'T.' Enter the number of digits used to encode the time step: in case of 'T001,' enter '3.' If the data are not time course data proceed to Step 4.

4| Enter the number of *z*-slices.

5| Enter the number of digits used for *z*-slice coding. The *z*-stack number must be at the end of the filename before the image format suffix, for instance '...001.png.'

6| Select the first image file of channel 1 ('green' channel).

7| Select the first image file of channel 2 ('blue' channel).

8| Enter the directory in which the converted data will be saved. The software then starts the image file conversion. If time course data are used, directories named according to the time step will be generated within the directory defined and contain the data for each time step. Otherwise, the converted images are saved directly in the directory specified.

Performing data analysis

9| Start the software '2pisaloader.'

10| In the menu 'Data', select 'Start data analysis.'

? TROUBLESHOOTING

11| Select the directory that contains the image data. Depending on the content of the selected directory, the software will automatically determine whether a single set or multiple data sets are to be analyzed: If the selected directory contains subdirectories with image files, all subdirectories are processed. If no subdirectories are present, the analysis is limited to the files in the selected directory. As the program counts the number of files in each directory to determine the size of the *z*-stack, it is important that only the relevant images files are in the directory named following the convention described above (see 'Data preparation').

12| Enter the filename prefix. The prefix has to be the same for all images files within the selected directory and subdirectories. Subsequently, the fully automated segmentation and analysis process is started and does not require any further user interaction.

? TROUBLESHOOTING

Results

13| Locate the segmentation results. These will be saved in the same directories as the original images with the filename prefix 'result' followed by the *z*-slice identifier equivalent to that of the original image, for instance for 'originalimage100.png,' 'result100.png.' In addition to the resulting image files, each directory will contain a file ('Results.txt') providing detailed interaction statistics, such as the number of interfacing cells/tissue components, interface area relative to total surface area, interface area per interfacing component, etc. If multiple data sets/directories are analyzed simultaneously, the top-level directory will contain a file ('AllResults.txt') that combines the results of all data sets.

14| Directly read these files and/or import to statistics/spreadsheet software for further analysis or visualization.

● TIMING

The analysis time strongly depends on the size and composition of the data sets and the computer hardware. The approximate duration of the bone–osteoclast interaction analysis with 512 × 512 × ~20 data sets on an Intel Xeon 3.0 GHz/16 GB workstation running 64-bit Linux is in the order of several minutes.

? TROUBLESHOOTING

Step 10: Manual parameter optimization

Although the default settings for the fully automated processing of the data worked well for all data sets we tested, the user can override the default settings and manually adjust/set the parameters 'slope constant,' 'threshold value' and 'minimal object size' to account for specific data features and optimize the accuracy of the analysis. Manual parameter selection can be enabled in the 'Settings' menu.

Step 12: Memory limitations

If large image data sets containing large numbers of objects are analyzed, the memory of standard 32-bit hardware (maximum 4 GB memory) may be insufficient and the analysis process might be terminated. Although it is not possible to precisely determine the memory requirement for a given image size, because it partially depends on the number of image objects processed in the connected component module, a rough estimate is that data sets of size ~250 × 250 × 10 (width × length × height) with a number of components similar to that present in the lymphocyte example can in most cases be analyzed on 32-bit hardware, whereas data sets equal to or larger than ~500 × 500 × >20 (as is the case for the bone–osteoclast data) are likely to require more memory. As an alternative to using 64-bit hardware with sufficient memory (~8 to 16 GB), the data sets can also be split into smaller subsets that are then analyzed separately.

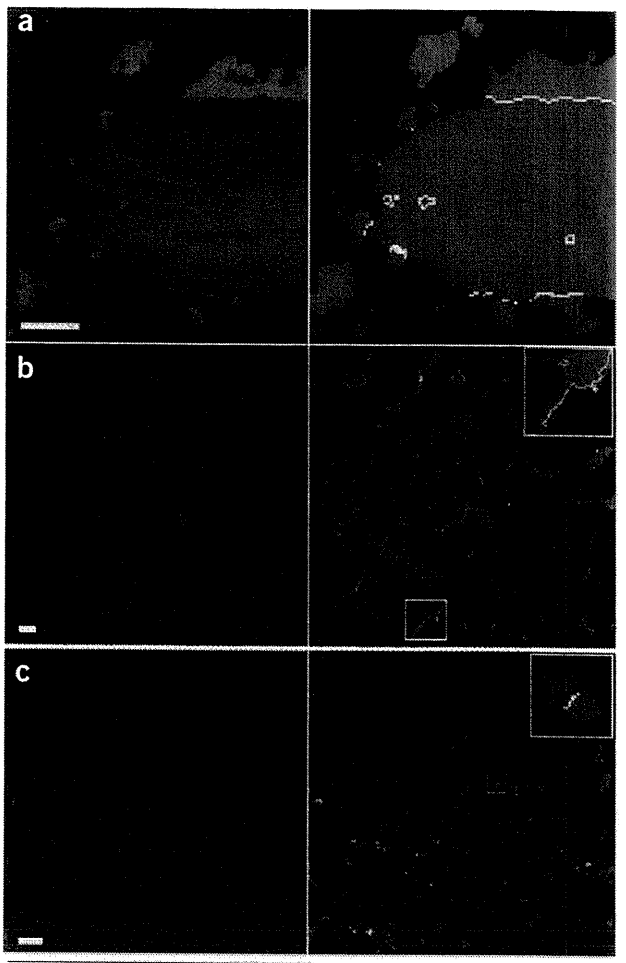

Figure 4 | Segmentation example results. Left column: original images; right column: segmentation results. (**a**) Bone–osteoclast interaction (osteoclasts: green; bone: blue; interacting osteoclasts: red). (**b**) Dendritic cells (DCs, green/red) and fiber network (blue) in lymph nodes (white: interface area). Analysis of the whole 3D data set reveals that 22% of the DC surface is attached to fibers. (**c**) T–B-cell interaction in lymph nodes (T cells: green/red; B cells: blue). Scale bars = 10 μm. All animal procedures used in this study have been approved by the Animal Care and Use Committee, NIAID, NIH.

ANTICIPATED RESULTS

Analysis of interactions of osteoclasts and bone tissue

In the first and main example application we show here, the interacting components of interest are bone tissue and osteoclasts (for illustrations see **Figs. 1, 3** and **4a**). The extent of the interface area between osteoclasts and bone provides a measure of osteoclast activity. Generated by fusion of multiple monocyte-derived precursor cells, osteoclasts in their mature state resorb bone tissue, thereby acting as important components for bone and calcium homoeostasis[17]. To quantify the influence of pathological conditions, therapeutic interventions or experimental conditions on bone metabolism, previous studies have relied on methods such as bone densitometry or the use of manual or semi-automated image analyses[7–9, 18] based on a bone histomorphometry standard developed by Parfitt *et al.*[19]. Recent data from our laboratory suggested that the lipid mediator S1P and its receptor $S1P_1$ might have important roles in regulating osteoclast generation by controlling the rate of osteoclast precursor detachment from the bone surface before mature osteoclast formation[12]. To assess the influence of the immunomodulatory drug FTY720 (a blocker of S1P/$S1P_1$ function) on bone metabolism, we developed this protocol to analyze microscopy images of osteoclasts interacting with bone tissue and quantified the osteoclast attachment ratio, which is defined as the ratio of the interface area between osteoclasts and bone tissue and the total bone surface.

We found that this ratio changes from ~0.3 in control to 0.6 in ovariectomized mice that develop osteopenia due to unbalanced osteoclast activity and that treatment of these animals with FTY720 reduces the osteoclast attachment to bone almost to normal levels (~0.35, $P = 0.0006$). Evaluation of the influence of $S1P_1$ function on osteoclast function revealed a decrease in the osteoclast attachment ratio from ~0.6 in wild-type to ~0.44 in $S1P_1^{-/-}$ knockout mutants ($P = 0.0003$). (For further details on the experimental design and biological implications of the actual experiments, see reference 12.)

Additional example data

Although the bone–osteoclast application deals with the interaction of relatively large cells with large tissue structures, the protocol can also be used to analyze interaction behavior when the relevant dimensions of the biological objects are much smaller. Examples are image data showing dendritic cell–fibroblast reticular network attachment and T–B lymphocyte interaction. Typical results that can be expected from analyzing such data are shown in **Figure 4**.

Note: Supplementary information is available via the HTML version of this article.

ACKNOWLEDGMENTS This research was supported by the Intramural Research Program of NIAID, NIH. M.I. was supported by a fellowship grant from the International Human Frontier Science Program.

AUTHOR CONTRIBUTIONS F.K. designed, implemented and tested the method. F.K., M.M.-S. and R.N.G. prepared the paper. M.M.-S. and R.N.G. supervised the project. M.I., H.Q., M.B., J.G.E. and F.K. generated and provided experimental data.

Published online at http://www.natureprotocols.com.
Reprints and permissions information is available online at http://npg.nature.com/reprintsandpermissions.

1. Germain, R.N. *et al.* An extended vision for dynamic high-resolution intravital immune imaging. *Semin. Immunol.* **17**, 431–441 (2005).
2. Stoll, S., Delon, J., Brotz, T.M. & Germain, R.N. Dynamic imaging of T cell–dendritic cell interactions in lymph nodes. *Science* **296**, 1873–1876 (2002).
3. Xu, X., Meier-Schellersheim, M., Yan, J. & Jin, T. Locally controlled inhibitory mechanisms are involved in eukaryotic GPCR-mediated chemosensing. *J. Cell Biol.* **178**, 141–153 (2007).
4. Fisher, D.T. *et al.* Hurdles to lymphocyte trafficking in the tumor microenvironment: implications for effective immunotherapy. *Immunol. Invest.* **35**, 251–277 (2006).
5. Nishida, H. & Okabe, S. Visualization of synapse–glia dynamics. *Brain Nerve* **59**, 755–761 (2007).

6. Wollman, R. & Stuurman, N. High throughput microscopy: from raw images to discoveries. *J. Cell Sci.* **120**, 3715–3722 (2007).
7. Yamada, C. *et al.* The murine glucagon-like peptide-1 receptor is essential for control of bone resorption. *Endocrinology* **149**, 574–579 (2008).
8. Nakamura, T. *et al.* Estrogen prevents bone loss via estrogen receptor alpha and induction of Fas ligand in osteoclasts. *Cell* **130**, 811–823 (2007).
9. Lee, S.H. *et al.* v-ATPase V0 subunit d2-deficient mice exhibit impaired osteoclast fusion and increased bone formation. *Nat. Med.* **12**, 1403–1409 (2006).
10. Castellino, F. *et al.* Chemokines enhance immunity by guiding naive CD8+ T cells to sites of CD4+ T cell–dendritic cell interaction. *Nature* **440**, 890–895 (2006).
11. Henrickson, S.E. *et al.* T cell sensing of antigen dose governs interactive behavior with dendritic cells and sets a threshold for T cell activation. *Nat. Immunol.* **9**, 282–291 (2008).
12. Ishii, M. *et al.* Sphingosine-1-phosphate mobilizes osteoclast precursors and regulates bone homeostasis. *Nature* **458**, 524–528 (2009).
13. Qi, H., Cannons, J.L., Klauschen, F., Schwartzberg, P.L. & Germain, R.N. SAP-controlled T–B cell interactions underlie germinal centre formation. *Nature* **455**, 764–769 (2008).
14. Sezgin, H. & Sankur, B. Survey over image thresholding techniques and quantitative performance evaluation. *J. Electron. Imaging* **13**, 146–168 (2004).
15. Suzuki, K., Horiba, I. & Sugie, N. Linear-time connected-component labeling based on sequential local operations. *Comput. Vis. Image Underst.* **89**, 1–23 (2003).
16. Kervrann, C. & Trubuli, A. An adaptive window approach for Poisson noise reduction and structure preserving in confocal microscopy. *IEEE Int. Symp. Biomed. Imaging* **1**, 788–791 (2004).
17. Bar-Shavit, Z. The osteoclast: a multinucleated, hematopoietic-origin, bone-resorbing osteoimmune cell. *J. Cell. Biochem.* **102**, 1130–1139 (2007).
18. Wada, T. *et al.* The molecular scaffold Gab2 is a crucial component of RANK signaling and osteoclastogenesis. *Nat. Med.* **11**, 394–399 (2005).
19. Parfitt, A.M. *et al.* Bone histomorphometry: standardization of nomenclature, symbols, and units. Report of the ASBMR Histomorphometry Nomenclature Committee. *J. Bone Miner Res.* **2**, 595–610 (1987).

Visualization and Identification of IL-7 Producing Cells in Reporter Mice

Renata I. Mazzucchelli[1¤a], Søren Warming[2¤b], Scott M. Lawrence[3], Masaru Ishii[4¤c], Mehrnoosh Abshari[3¤d], A. Valance Washington[5¤e], Lionel Feigenbaum[3], Andrew C. Warner[3], Davis J. Sims[3], Wen Qing Li[1], Julie A. Hixon[1], Daniel H. D. Gray[6], Benjamin E. Rich[7], Matthew Morrow[8], Miriam R. Anver[3], James Cherry[9], Dieter Naf[3], Lawrence R. Sternberg[3], Daniel W. McVicar[5], Andrew G. Farr[10], Ronald N. Germain[4], Keith Rogers[3], Nancy A. Jenkins[2¤f], Neal G. Copeland[2¤f], Scott K. Durum[1]*

1 Laboratory of Molecular Immunoregulation, Cancer and Inflammation Program, Center for Cancer Research, National Cancer Institute, National Institute of Health, Frederick, Maryland, United States of America, **2** Mouse Cancer Genetics Program, National Cancer Institute, Frederick, Maryland, United States of America, **3** Laboratory Animal Science Program (LASP), Science Applications International Corporation (SAIC), Cancer Research Center, National Cancer Institute, Frederick, Maryland, United States of America, **4** Lymphocyte Biology Section, Laboratory of Immunology, National Institute of Allergy and Infectious Diseases, National Institutes of Health, Bethesda, Maryland, United States of America, **5** Laboratory of Experimental Immunology, Cancer and Inflammation Program, Center for Cancer Research, National Cancer Institute, National Institute of Health, Frederick, Maryland, United States of America, **6** The Walter and Eliza Hall Institute of Medical Research, Parkville, Victoria, Australia, **7** Department of Dermatology, Brigham and Women's Hospital, Boston, Massachusetts, United States of America, **8** Human Retrovirus Section, Vaccine Branch, Center for Cancer Research NCI, Frederick, Maryland, United States of America, **9** Gene Expression Laboratory, SAIC-Frederick, Inc., NCI-Frederick, Frederick, Maryland, United States of America, **10** Department of Immunology, University of Washington, Seattle, Washington, United States of America

Abstract

Interleukin-7 (IL-7) is required for lymphocyte development and homeostasis although the actual sites of IL-7 production have never been clearly identified. We produced a bacterial artificial chromosome (BAC) transgenic mouse expressing ECFP in the *Il7* locus. The construct lacked a signal peptide and ECFP (enhanced cyan fluorescent protein) accumulated inside IL-7-producing stromal cells in thoracic thymus, cervical thymus and bone marrow. In thymus, an extensive reticular network of IL-7-containing processes extended from cortical and medullary epithelial cells, closely contacting thymocytes. Central memory CD8 T cells, which require IL-7 and home to bone marrow, physically associated with IL-7-producing cells as we demonstrate by intravital imaging.

Citation: Mazzucchelli RI, Warming S, Lawrence SM, Ishii M, Abshari M, et al. (2009) Visualization and Identification of IL-7 Producing Cells in Reporter Mice. PLoS ONE 4(11): e7637. doi:10.1371/journal.pone.0007637

Editor: Derya Unutmaz, New York University School of Medicine, United States of America

Received August 7, 2009; **Accepted** September 22, 2009; **Published** November 10, 2009

Funding: This project has been funded in whole or in part with federal funds from the National Cancer Institute, National Institutes of Health, under contract N01-CO-12400. The content of this publication does not necessarily reflect the views or policies of the Department of Health and Human Services, nor does mention of trade names, commercial products, or organizations imply endorsement by the U.S.Government. R.I.M. is a recipient of a FIRC-Fondazione Italiana Ricerca sul Cancro- fellowship. M.I. received Human Frontier Science Program Postdoctoral Fellowship. The funders had no role in study design, data collection and analysis, decision to publish, or preparation of the manuscript.

Competing Interests: The authors have declared that no competing interests exist.

* E-mail: durums@ncifcrf.gov

¤a Current address: Laboratory of Gene Therapy and Primary Immunodeficiency, San Raffaele Telethon Institute for Gene Therapy, HSR-TIGET, Milano, Italy,
¤b Current address: Genentech, Inc., Department of Molecular Biology, South San Francisco, California, United States of America
¤c Current address: Laboratory of Biological Imaging, Immunology Frontier Research Center, Osaka University, Osaka, Japan
¤d Current address: Twinbrook Flow Cytometry Facility, Lockheed Martin Contractor, RTB/NiAID/NIH, Rockville, Maryland, United States of America
¤e Current address: Department of Biology, University of Puerto Rico Recinto Mayaguez, Mayaguez, Puerto Rico
¤f Current address: Institute of Molecular and Cell Biology, Proteos, Singapore

Introduction

Interleukin-7 (IL-7) is required for T cell development and survival (reviewed in Khaled and Durum [1]) as first appreciated from the severe lymphopenia observed in $IL7^{-/-}$ and $IL\text{-}7R^{-/-}$ mice [2,3], then in comparable deficiencies in humans found to lack components of the IL-7 receptor [4] (reviewed in Puel and Leonard [5]).

Although IL-7 plays a critical role in the thymus and peripheral T cell homeostasis, stromal cells producing IL-7 have never been precisely identified. This was mainly due to the low abundance of message and protein (as we demonstrate in this study). Since IL-7 was first described in 1988, a number of studies have detected *Il7* message in various tissues using Northern blot analysis or RT-PCR. These *Il7* mRNA-expressing tissues include human and mouse thymus and spleen [6,7], mouse kidney [6], mouse fetal thymus [8–11], mouse fetal intestine and liver [11,12] and adult human liver [13]. In our own lab, we have verified the presence of *Il7* mRNA by RT-PCR from homogenized mouse tissue including thymus, spleen, lymph nodes and bone marrow (R.I. Mazzucchelli, unpublished observations). RT-PCR has also been used to identify *Il7* mRNA in specific cell populations including those derived from human tonsillar germinal centers [14], fetal thymus stromal cells [15], mouse bone marrow stromal cells [16], mouse and human keratinocytes [17–20], human intestinal epithelial cells [21,22], human follicular dendritic cells and vascular cells [23], human mature peripheral dendritic cells [14,24] and human platelets [25].

There are a few reports identifying sites of *Il7* mRNA production using in situ hybridization which indicate transcription in human postnatal thymus [26] and mouse embryonic, postnatal and adult thymus [27,28], mouse and human keratinocytes [17] and human intestinal mucosa [21]. In mouse thymus, *Il7* mRNA expression was reported in one study to decline in adulthood to below the level of detection by in situ hybridization [28]. In another study [27], it was reported that the adult thymus sections required 6 weeks of exposure to the probe to develop a clear signal. Yet despite IL-7 being virtually undetectably by in situ hybridization in the adult, it is clear that the adult mouse thymus produces biologically significant IL-7 based on thymic reconstitution experiments that show a dramatic difference between IL-$7^{-/-}$ compared to wild type thymus.

The production of *Il7* mRNA does not guarantee that a cell produces the protein because posttranscriptional controls can block mRNA translation. This is the case for IL-15, a cytokine related to IL-7 and with similar homeostatic activities. Production of IL-15 is regulated not only by transcription and mRNA stability, like most cytokines, but also at the translation level (reviewed by Tagaya et al. [29] The 5′ untranslated region of *Il15* mRNA contains 10 ATG sequences which strongly inhibit translation. Similarly, the 5′ untranslated region of murine *Il7* mRNA contains 8 ATG sequences and has also been shown to greatly inhibit translation in Cos-7 cells [6]. In our laboratory, we analyzed 20 stromal cell lines from mouse thymus, bone marrow and spleen, all expressing *Il7* mRNA, but only two produced enough protein to be detectable by ELISA or bioassay (R.I. Mazzucchelli, unpublished observations) suggesting that there could be translational inhibition of IL-7 production.

Immunohistochemical detection of IL-7 protein in human tissue has been reported by several groups. Although not reported in human thymus, immunohistochemical reactions have been seen in healthy human intestinal epithelial cells [21], human follicular dendritic cells[23], human *Schistosoma mansoni* infected skin [20], human Warthin's tumor [30], healthy human liver [13] and lymph nodes of AIDS patients [31]. The specificity of such staining can be more easily assessed using mouse tissues because of the availability of IL-$7^{-/-}$ mice. There are some early reports of positive immunohistochemical reactions for murine IL-7 in adult bone marrow [32], fetal liver tissue [33], embryonic [9,34] and adult thymus [33], all preceding the availability of IL-$7^{-/-}$ tissues to verify specificity. An experienced veterinary pathology laboratory at NCI tested six different commercial and non-commercial anti-IL-7 monoclonal and polyclonal antibodies, following published protocols and optimizing our own protocols. No specific reactions were found in any mouse lymphoid or non-lymphoid tissues, some of those data are shown in the results.

Because the identification of IL-7-producing cells has been so difficult, we have developed a novel strategy to amplify the signal from these cells and allow direct visualization of such cells in tissues. A bacterial artificial chromosome was modified to introduce a fluorescent reporter gene into the *Il7* locus that should be trapped inside the producing cells. Transgenic mice prepared using this reporter construct enabled, for the first time, identification of the cells that produce IL-7 in thymus and bone marrow.

Results

IL-7 expression in thymus is below the level of detection by immunohistochemistry and in situ hybridization

We and others (personal communications: D. Klug, NCI; C. Mackall, NCI; C. Willis, Amgen) have tested a number of polyclonal and monoclonal anti-IL-7 antibodies and failed to observe a positive reaction in thymic tissue (Table 1). Some of these antibodies are effective in western blotting or blocking the biological activity of IL-7. Immunohistochemical methods, used extensively in our institute, were applied to thymic tissue from C57BL/6, Rag2$^{-/-}$, and as a positive control, mice overexpressing IL-7 under control of the *K14* promoter. Thymus tissue from IL-$7^{-/-}$ mice was used as a negative control. Several protocols for tissue preparation were evaluated that showed staining with the positive control (transgenic overexpression of IL-7), but all were consistently negative with normal thymus, except two that apparently gave non-specific staining based on a signal from IL-$7^{-/-}$ thymic material.

Because mRNA could be more readily detectable than protein if there were impediments to translation in case IL-7 synthesis were subjected to translational or post-translational control, we examined expression of *Il7* mRNA in the thymus by in situ hybridization. Three different set of probes were synthesized and tested on both frozen or paraffin embedded tissue. The same mouse strains (C57BL/6, Rag2$^{-/-}$ and K14) that failed to show detectable IL-7 by immunohistochemistry also failed to give a signal for *Il7* mRNA by in situ hybridization (data not shown).

Because two routine laboratory techniques, immunohistochemistry and in situ hybridization, failed to localize IL-7 production in thymus, we quantified *Il7* mRNA expression in thymus by real time PCR. Total mRNA was extracted from thymi harvested from C57BL/6, Rag2$^{-/-}$ and K14 mice and immediately placed into RNAlater to protect the mRNA from degradation. Following RNA extraction, RT-real time PCR was performed to compare

Table 1. Immunohistochemistry fails to detect IL-7 in murine thymus.

	Antibody	Notes	Results
1	Rabbit Polyclonal IgG[1]	Epitope mapping at the N-terminus	Negative
2	Goat Polyclonal IgG[2]	Epitope mapping at the C-terminus	Negative
3	Goat Polyclonal IgG[3]	Purified by affinity chromatography	Negative
4	Monoclonal Rat IgG[4]	Purified by affinity chromatography	Negative
5	Rabbit Polyclonal IgG[5]	Purified by affinity chromatography and biotinylated	Negative
6	Monoclonal Mouse IgG[6]	Effective blocking in vivo and in vitro	Negative

Several commercial and non-commercial anti-IL-7 antibodies were tested at various concentration and fixation conditions and evaluated by a veterinary pathologist. None of them showed positive staining of normal thymus although several reacted non-specifically with an IL$7^{-/-}$ mouse tissue. Sources: 1-Santa Cruz, 2-Santa Cruz, 3-R&D, 4-R&D, 5-Peprotech, 6-Amgen.

doi:10.1371/journal.pone.0007637.t001

the expression of *Il7* mRNA to the housekeeping genes *Gapdh* and *18 s*. Data in Figure 1A show that mRNA expression of *Il7* in the whole thymus was 1–2 orders of magnitude lower than *Gapdh* and 4–5 orders of magnitude lower than *18 s* mRNA. This extremely low level of *Il7* mRNA expression in thymus could account for the failure to detect it by in situ hybridization, and in turn the failure to detect the protein by immunohistochemistry, although other technical explanations could also account for it, if for example none of the six anti-IL-7 antibodies are suitable for immunohistochemistry.

Cell sorting of mouse stromal cell subsets

Because visualization of IL-7 producing cells in thymus was not achievable by immunohistochemistry or in situ hybridization we aimed to physically purify subsets of thymic stromal cells and quantitate their content of *Il7* mRNA. Table 2 lists the stromal cell subsets known to be present in thymus (dendritic cells, myeloid-derived cells, cortical epithelial cells, medullar epithelial cells, fibroblasts and endothelial cells) and the antibodies used to isolate them. After cell sorting, mRNA was extracted, reverse transcribed and an absolute quantification for *Il7* expression was performed by real time PCR. The amount of *Il7* mRNA was very low (Figure 1B), fewer than one molecule per cell in cortical and medullar epithelial cells, whereas fibroblasts and endothelial cells expressed about half a molecule per cell, and dendritic and myeloid cells showed virtually no signal. Because several thymic stromal subsets expressed *Il7* mRNA, this approach did not reveal a single likely source of IL-7 protein; moreover, IL-7 could be

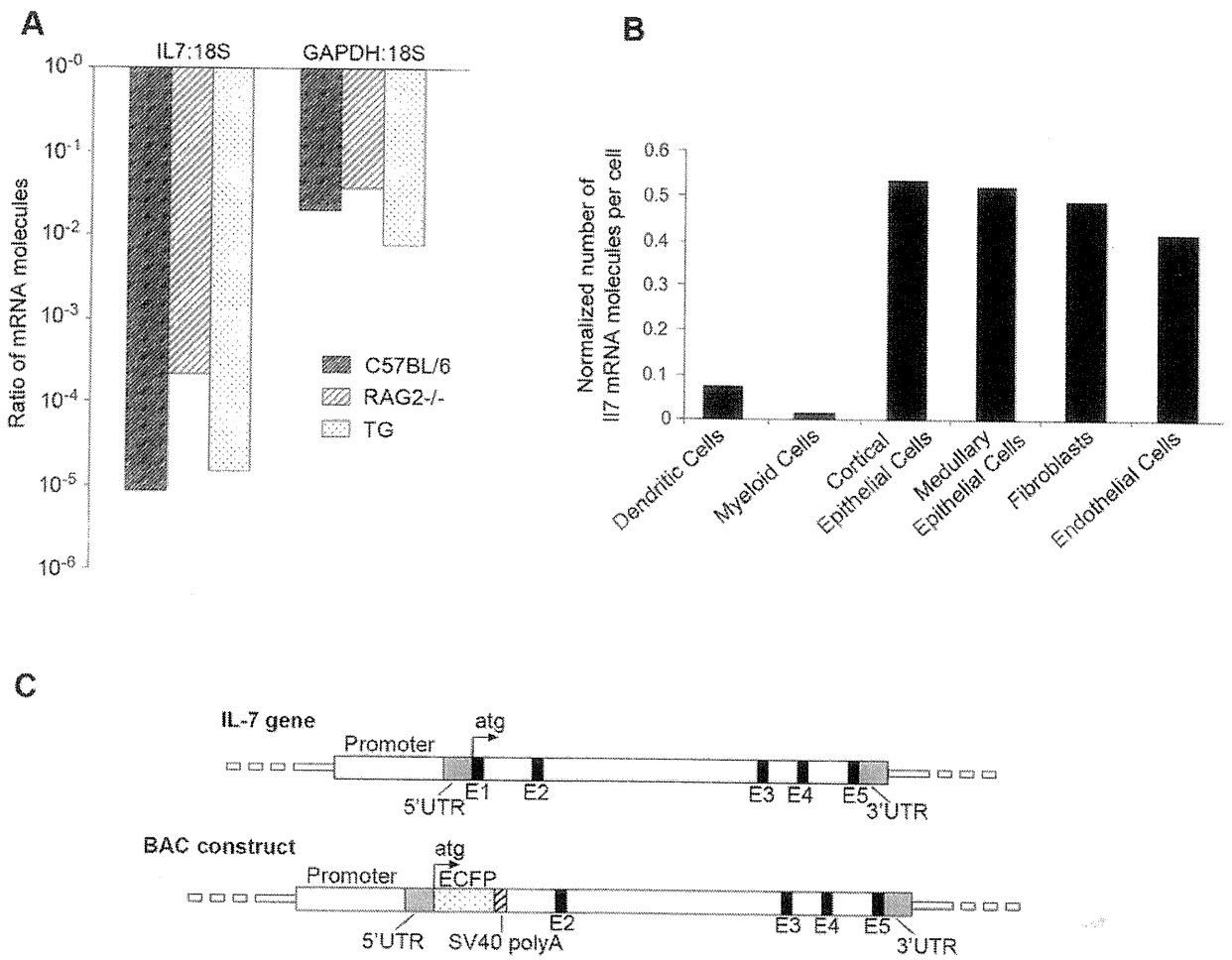

Figure 1. Il7 mRNA expression in different mouse strains and in thymic stromal cell subtypes. A. Thymi from C57BL/6, Rag2$^{-/-}$ and transgenic (TG) mice expressing IL-7 under control of the K14 promoter were analyzed for levels of *Il7* and *Gapdh* expression normalized to *18 s*. Wild type and even the transgenic mice expressed very low relative levels of *Il7* mRNA, while the Rag2$^{-/-}$ showed somewhat more, presumably because the thymus is enriched for stromal cells. *Gapdh* was expressed at a comparable level among all the strains. Data are the mean of three mice, no standard deviations are shown because ratios were used in the calculations. **B.** Quantification of *Il7* mRNA molecules in thymic stromal cells. Stromal cell subsets were sorted using specific surface markers (Table 1B). RNA was extracted and absolute real time PCR quantification was performed. *Il7* mRNA expression was normalized to *Hprt* mRNA expression for each subset. The data shown is representative of at least 2 separations for each subset. **C.** BAC construct for the IL7promECFP transgenic mouse. The wild type murine *Il7* gene is represented in the upper part of the figure. A BAC containing the mouse *Il7* gene (lower part of the figure) was modified and used to create the transgenic mouse. The exon 1 sequence, encoding the signal peptide was replaced with the *Ecfp* cDNA sequence starting after the ATG start site. The production of ECFP would thus be driven by the *Il7* promoter in IL-7 producing cells. Elimination of the signal peptide was intended to cause ECFP to accumulate inside IL-7 producing cells, enhancing visualization.

doi:10.1371/journal.pone.0007637.g001

Table 2. Specific cell markers for thymic stromal cell subsets.

Stromal Cell Subset	CD45.2	CD11c	EpCAM	Ly51	MTS-15	CD31
			G8.8a	CDR1		MTS-12
Dendritic Cells	+	high				
Myeloid-derived Cells	+	Low/−				
Cortical Epithelial Cells	−		+	+		
Medullary Epithelial Cells	−		+	−		
Fibroblasts	−		−		+	
Endothelial Cells	−		−		+/−	+

These markers were chosen to separate each specific stromal cell subtype by cell sorting (adapted from Gray et al. [48]). The same markers were also used in immunohistochemistry as shown in Figure 4.
doi:10.1371/journal.pone.0007637.t002

regulated translationally, like the related cytokine IL-15 [29]. For these reasons, the production of *Il7* mRNA by a cell type would not prove that the cell made the protein.

Visualization of IL-7 expression by IL7promECFP BAC transgenic mouse

To visualize IL-7 producing cells, we created a BAC transgenic mouse expressing a cyan fluorescent protein (ECFP) under the control of the *Il7* promoter and any other cis regulatory elements contained in a BAC. Using recombineering techniques, we inserted the *ECFP* cDNA sequence immediately after the ATG start site of *Il7*, replacing exon 1 (Figure 1C and S1). The large 5′ untranslated region was retained since this had been shown to inhibit translation of *Il7*, and we aimed to perturb natural regulation as little as possible. Since exon 1 encodes part of the signal peptide for IL-7, elimination of this sequence should cause ECFP to accumulate inside producing cells and enhance visualization. In addition, the splice donor GT sequence from intron 1 was deleted to prevent interference from splicing. Three founder lines of mice were produced and all showed similar expression patterns as will be discussed. The fluorescence emission of ECFP from tissues was relatively weak using the setup on our fluorescent microscope (although it was very bright in the two photon microscope to be discussed later). The signal was enhanced using an antibody against ECFP followed by a fluorescent secondary antibody to generate the images shown–no signal was detected in control tissues from non-transgenic mice.

ECFP expression was detected in stromal cells in thymus and bone marrow (Figures 2, 3, 4 and 5). Moreover, cervical thymus showed readily detectable levels of ECFP expression (Figure 6). In the thoracic thymus, ECFP positive cells were present in both cortex and medulla, although the pattern of expression was different (Figure 2A). In the medulla, the cell bodies containing ECFP were relatively infrequent, however an extensive network of processes extended from the cell bodies and most thymocytes were in close contact to such a process. In the cortex, ECFP positive cells appeared to envelop thymocytes, like a basket of fruit.

ECFP-positive cells were not visible in either spleen or lymph nodes of all three BAC transgenic strains - this negative finding was verified using several fluorescence microscopy systems. We also did not observe ECFP-positive cells in any other tissues examined including gut, lung, skin and brain; platelets isolated from blood were also negative. Thus, although most peripheral T cells require IL-7 for survival, we could not observe IL-7 production in the secondary lymphoid organs. Quantitative PCR was used to compare reporter expression with that of endogenous *Il7* (data not shown). The results indicate that reporter transcripts were well expressed in thymus and bone marrow where we had visualized the reporter protein. However, the reporter was only very slightly expressed in spleen and lymph node compared to *Il7*. The basis of this discrepancy will be discussed.

Cortical and medullar epithelial cells produce IL-7 in thymus

Thymic tissue from IL7promECFP BAC transgenic mice was stained using the antibodies specific for stromal cell subsets, previously used for cell sorting. Ly51 (CDR1) is a specific marker for cortical epithelial cells. Double staining of thymic tissue using anti-EGFP Ab and anti-Ly51 Ab revealed a co-localization of ECFP and Ly51 signal (Figure 3A, left panel and Figure 3B) identifying cortical epithelial cells as IL-7 producing cells. Staining with anti-EpCAM (G8.8a) Ab, a marker specific for both cortical and medullar epithelial cells, shows that some of the EpCAM positive cells in the medullar region are also ECFP positive, suggesting that medullar epithelial cells also produce IL-7 (Figure 3A, right panel).

The expression of IL-7 in cortical and medullar epithelial cells was confirmed by staining the thymic tissue with a panel of anti-keratin antibodies. In particular, ECFP co-localized with keratin-8 and keratin-14, two prominent cortical and medullar markers, respectively (Figure 4A and 4B). Co-localization is also present for ECFP and keratin-5, a marker mainly expressed in medulla, but also present in cortical cells (Figure 4A).

In thymus, fibroblast, endothelial cells, dendritic and myeloid-derived cells did not express ECFP since there was no co-localization with MTS-15, CD31, CD45.2 or CD11c, respectively (Figure S2).

Recently, cervical thymus was identified and characterized in mice [35,36]. The tissue organization is quite reminiscent of the thoracic thymus and the cervical thymus has been shown to support T-cell development. Since cervical thymus plays a role in T-cell differentiation, we have analyzed the expression of IL-7 and found that IL-7 is present in this ectopic thymus. As seen for thoracic thymus, expression of IL-7 is more evident in cortex compared to medulla (Figure 6).

Bone marrow also contained ECFP-positive cells as noted above (Figure 5). The shape of these cells is reminiscent of epithelial cells in thymus, but further characterization was not possible due to the lack of specific markers for bone marrow stromal cell subsets.

Central memory T cells interact with IL-7 producing cells in bone marrow

The fluorescence of IL-7-producing cells could permit visualization of their interaction with T cells using intravital microscopy with

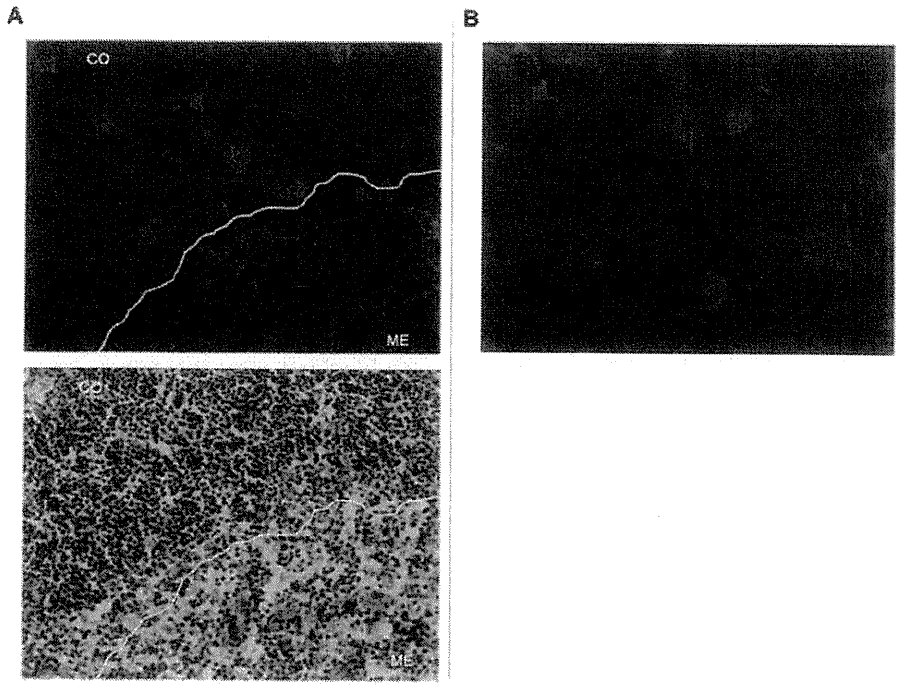

Figure 2. IL-7 is expressed in thymus. A. Expression of ECFP (or IL-7) by stromal cells in thymus is indicated by red fluorescence in the upper panel. The lower panel shows thymocytes by H&E staining on a sequential slide. The lines separate cortex (CO) from medulla (ME) in both pictures. The expression of IL-7 is higher in cortex compared to medulla and the pattern of expression is different between the two compartments. In the cortex, some IL-7 producing cells have a "basket-like" shape; in medulla the IL-7 producing cells are more dispersed and lacked the basket-like shape (magnification 200×). **B.** At higher magnification (1000×) it is possible to appreciate how the bodies of ECFP-positive cells are very infrequent compared to hematopoietic cells, but there are extensive reticular processes extending throughout the tissue. These reticular processes contain the ECFP protein and are in close contact with many thymocytes whose nuclei are visualized by DAPI (blue staining).
doi:10.1371/journal.pone.0007637.g002

two photon imaging. The thymus is not amenable to intravital microscopy because in the living mouse, lies over the beating heart and it cannot be isolated from the thoracic cavity. Bone marrow, on the other hand, can be imaged in the skull of the living mouse. It has been reported that central memory T cells (TCMs) express IL-7 receptor and require it for survival [37]. Since TCMs home to bone marrow [38], we asked whether these T cells might physically associate with IL-7-producing cells. TCMs were generated in vitro, labeled with CFSE and intravenously injected into ECFP positive mice. Intravital microscopy showed that TCMs homed to bone marrow as previously described. A number of TCMs showed stable interactions with IL-7 producing cells (see supplemental Movie S1 and Movie S2 which shows circles around several interactions), and analysis indicated approximately a 2.85 preference for the IL-7-producing cells (see supplemental Table S1). This suggests that IL-7 may be recognized during close physical contact between T cells and IL-7 producing cells.

This apparent attraction of TCMs to IL-7-expressing cells could be mediated by IL-7 itself. To test this possibility, we generated mice that were deficient in IL-7 but expressed the reporter. These mice were injected with CFSE labeled TCM cells and we monitored the number of cells that were present in bone marrow 24 hour later. The results showed no decrease of TCMs that initially entered in IL-$7^{-/-}$ compared to control mice, in fact the percentage was somewhat higher possibly because they lacked endogenous CD8 cells (Figure S3A and S3B). This suggests that IL-7 itself was not the attractant guiding TCMs to the IL-7-producing cell.

If the IL-7-producing cells also expressed a chemokine that attracted TCMs, these cells express CXCR4 and can be recruited and retained into bone marrow by CXCL12 [38]. However, injection of the CXCR4 antagonist AMD3100 into IL7-ECFP mice did block the early entry of TCM cells (Figure S3A and S3B) and immunofluorescence (data not shown). These data suggest that a ligand other than IL-7 and CXCL12 may be involved in guiding TCMs to the IL-7-producing stromal cells in bone marrow.

Discussion

IL-7 is essential for T cell development and homeostasis; however the cells that produce IL-7 have never been directly visualized by conventional immunohistochemistry due to the low level of expression. We employed a BAC transgenic strategy for detecting cells that produced ECFP from the *Il7* locus. The ECFP reporter construct was inserted in a large BAC, over 200 kbp in length, to insure fidelity of expression by the normal tissue specific regulatory elements. The IL-7-driven ECFP lacked a signal peptide resulting in accumulation in the cytosol, thereby enabling the visualizing of IL-7 producing cells. ECFP from the BAC did not interfere with IL-7 production from the endogenous gene, and thymic development appeared normal. Cells expressing ECFP were detected in thoracic thymus, cervical thymus and bone marrow.

In thymus, cortical epithelial cells contained the highest level and showed extensive dendritic branches containing ECFP in a reticular pattern. Since most cortical thymocytes were in close contact with an IL-7-containing branch, it suggested a short range, paracrine delivery of IL-7, possibly on the surface of the producing cell or nearby extracellular matrix. Some of these cortical

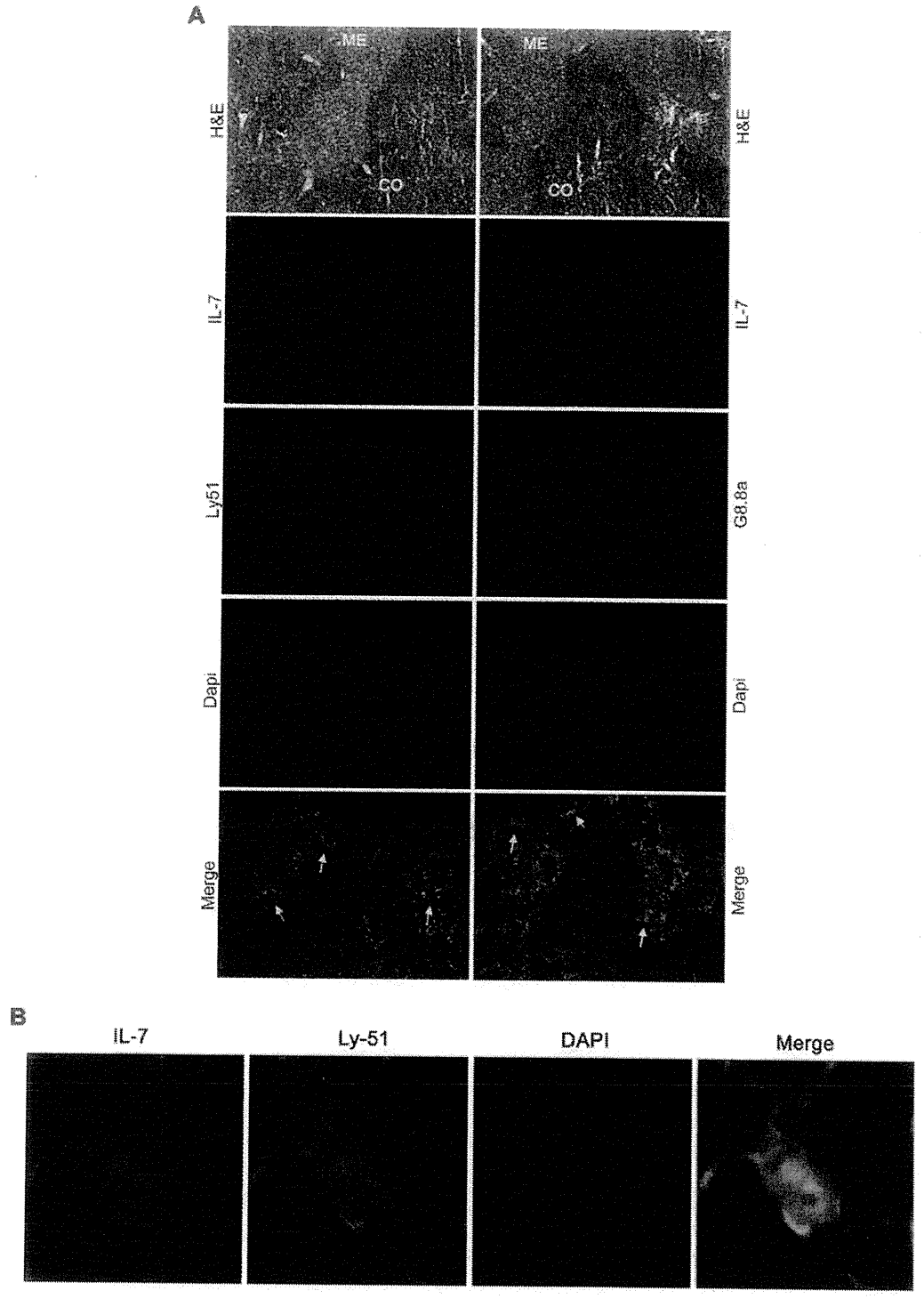

Figure 3. Cortical and medullary epithelial cells express IL-7 in thymus. A. Colocalization of ECFP-positive cells (red staining) with Ly51 and G8.8a (green staining) indicates the cortical cells and medullary epithelial cells, respectively, are responsible for production of IL-7 in thymus. H&E staining shows thymocyte distribution between cortex and medulla. Single color staining show the expression of ECFP (counterstained red), cortical Ly51 positive cells or medullary G8.8a positive cells (green), nuclei visualization by DAPI (blue). In the merged figures, the arrows indicate some cells with co-localization of red and green (yellow staining). Magnification 100×. **B.** Detail of the body of two cortical epithelial cells (magnification 400×). The yellow staining in the merged figure visualized the co-localization between ECFP (counterstained red) and the cortical marker Ly51 (green).
doi:10.1371/journal.pone.0007637.g003

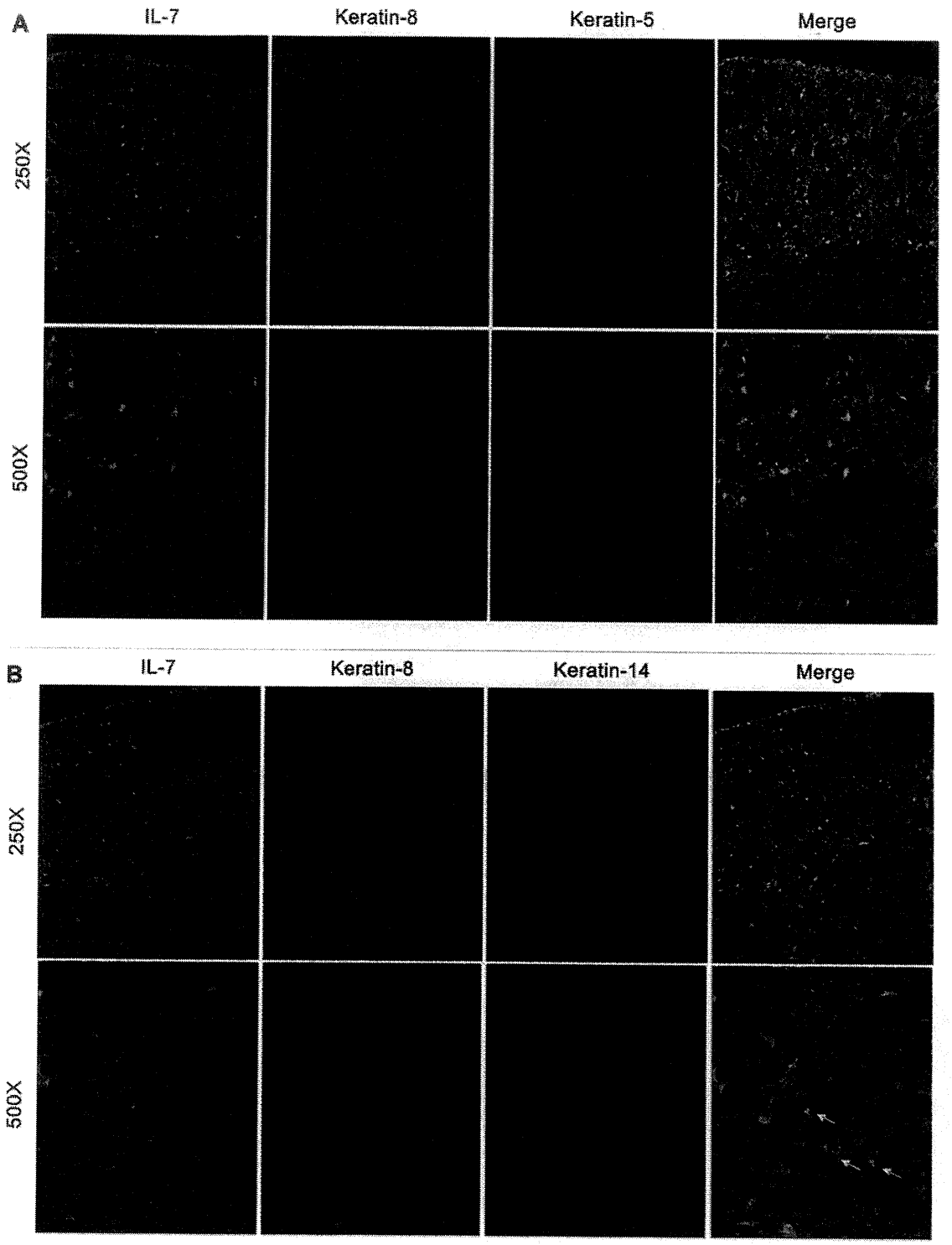

Figure 4. Cortical and medullary cell expression of IL-7 in thymic epithelial cells is confirmed by staining with different anti-keratin antibodies. A. ECFP (counterstained green) extensively co-localized with keratin-8 (red), a prominent cortical cell marker. To a less extent, co-localization is also present between ECFP (green) and keratin-5 (blue), a marker expressed to a much higher level on medullary epithelial cells than on cortical cells. Magnification 250× (left column) and 500× (right column) are shown. **B.** Co-localization between ECFP (green) and keratin-14 (blue), a prominent marker for medullary cells is shown in two different set of figures at different magnification (250×, left column and 500×, right column). Arrows in the merged figure highlight IL-7 producing cells positive for the keratin-14 medullary marker.
doi:10.1371/journal.pone.0007637.g004

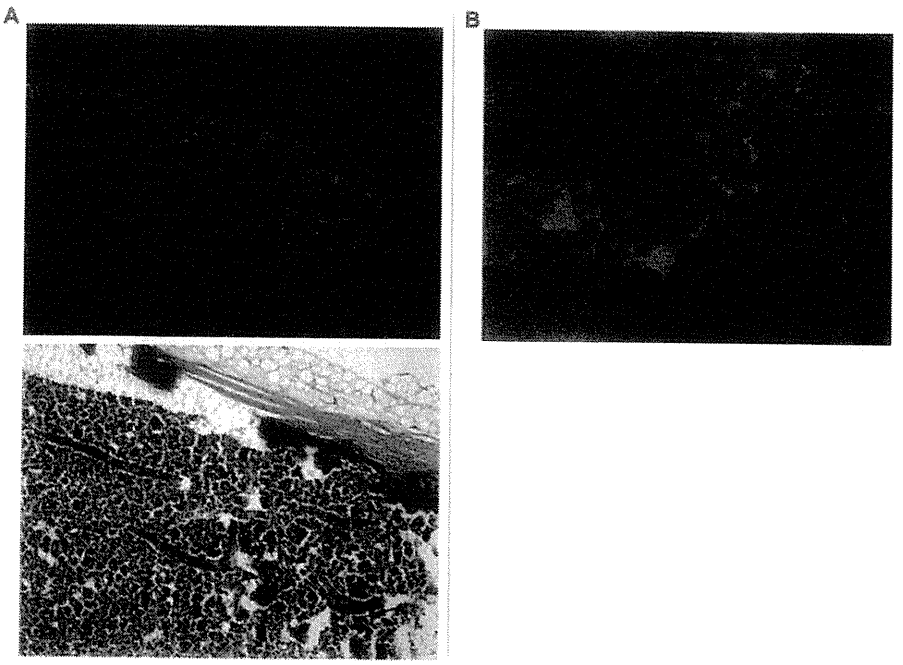

Figure 5. Bone marrow contains IL-7-producing cells. A. A section of femur shows that ECFP (counterstained red) is produced in bone marrow by stromal cells concentrated around vessels. The lower panel shows H&E staining of the same section. Magnification 100×. **B.** As also seen in thymus, bone marrow IL-7 producing cells expressed long dendrites that make extensive contacts with hematopoietic cells. Magnification 1000×.
doi:10.1371/journal.pone.0007637.g005

epithelial cells had a "basket-like" shape and appeared to envelop a number of thymocytes. Medullar epithelial cells also contained ECFP, but the amount was less than in the cortex. The cervical thymus, long noted in man, has only recently been reported in mouse [35,36]. The architecture of the cervical thymus also features cortical and medullar regions, and like the thoracic thymus, the production of ECFP was higher in the cortex.

Central memory T cells require IL-7 (reviewed in Bradley et al. [39]) and accumulate in bone marrow [38], and we show here that they can interact with IL-7 producers. IL-7 could participate in localizing TCMs in bone marrow because it has been shown to induce T cell adhesion by activating integrins [34,40]. The initial migration of OT-1 central memory cells to bone marrow was not reduced by IL-7 deletion (supplementary Figures S3A and S3B). Based on this experiment, we conclude that IL-7 is not chemotactic for these cells. The association of central memory cells with IL-7-producing cells is therefore more likely to be due to some other attractant that is also produced by these cells. We considered SDF-1 a candidate because central memory cells express its receptor, CXCR4, and SDF-1 is expressed in bone marrow. However an antagonist against CXCR4 did not interfere with this migration to bone marrow (supplementary Figures S3A and S3B). It therefore remains an important open question as to how central memory cells are attracted to IL-7-producing cells, and we hope that gene profiling the latter cells will offer some clues to this mechanism.

In the literature, the stromal cell types in bone marrow have not been characterized as extensively as those in thymus. One candidate for the IL-7 producing cell was the osteoblast which had been reported to produce IL-7 after culture in parathyroid hormone [41]. However, staining marrow sections from the IL7promECFP reporter mouse with antibodies against markers reported for osteoblasts (osteocalcin, osteopontin or SDF-1) failed to give specific staining as determined by an experienced immunohistochemistry service at NCI. These cells appear to be fragile, as is also the case with the thymic ECFP-expressing cells, most of which disintegrated when cell suspensions were made, despite the use of gentle enzymatic dissociation methods. In the future we hope to use laser capture to characterize these intriguing cells.

There was a lack of reporter signal in spleen, lymph node, gut, lung and skin, despite the established IL-7 requirement for mature T cells found in those sites. Naïve CD8 T cells require IL-7 and from other studies [42,43] and our own (Li et al. [44] and others not shown), this IL-7 encounter must occur within about four days following transfer into a recipient mouse and homing into lymphoid organs; without IL-7, naïve CD8 cells undergo cell cycle arrest and die. Unfortunately, our reporter was not expressed in these tissues when compared to expression of the endogenous *Il7* gene. This lack of expression (outside thymus and bone marrow) was not due to effects of the BAC integration site in the mouse genome since three different founders showed similar expression patterns. It was also not due to the placement of the reporter within the *Il7* gene, since insertion at either the 3′ or 5′ regions showed a similar mRNA expression pattern (data not shown). It was not due to toxicity of the reporter, since the expression of the endogenous *Il7* gene was not perturbed. One possibility is that the BAC contains the regulatory elements for expression in some, but not all cell types. If a regulatory element lies outside the BAC (see map in supplementary Figure S1), it would be over 80 kb upstream or downstream of the gene–a few genes have been reported with such distant sites, and although very unusual, *Il7* may be one. Another possibility is that the reporter RNA is unstable in some cells.

Having identified the principal thymic and bone marrow cells producing IL-7, a number of questions can now be addressed,

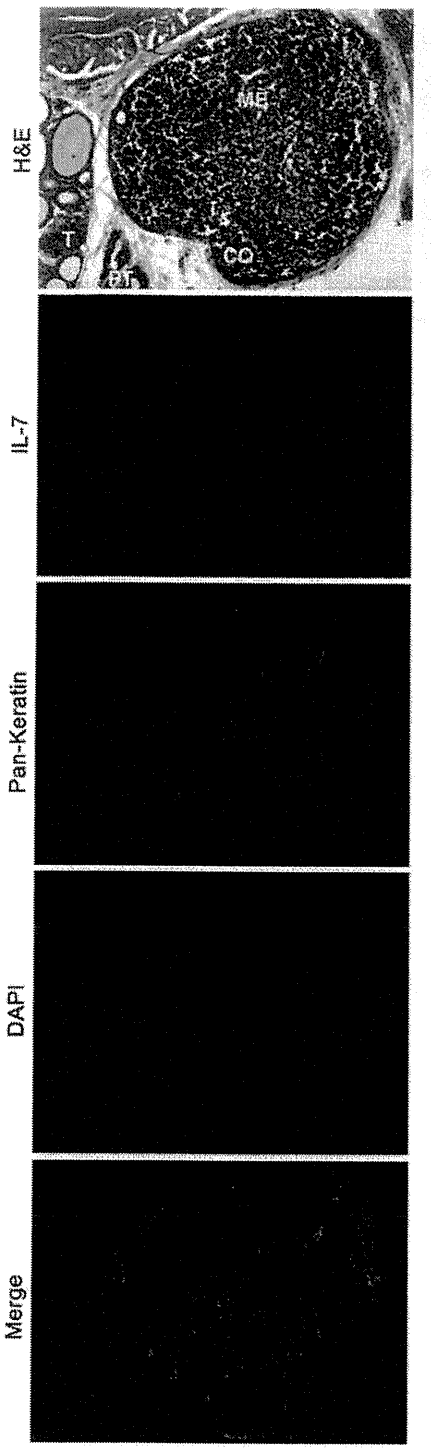

Figure 6. Cervical thymus contains IL-7-producing cells. H&E staining shows the cortical (CO) and medullary (ME) organization of the cervical thymus. ECFP (counterstained red) is mainly expressed in cortex by stromal cells (anti-pan keratin Ab, green staining). The wide spectrum anti-keratin antibody stains keratin-8 and keratin-5 among others, showing stromal cells present both in cortex and medulla. Magnification 200×. T, thyroid; PT, parathyroid.
doi:10.1371/journal.pone.0007637.g006

including their developmental origin, their fate in senescence, and their response to immune modulators. After IL-7 is released from these cells, it is proposed that its rate of consumption by T cells determines the size of the T cell pool (reviewed in Mazzucchelli and Durum [45]). However, to evaluate this concept of IL-7 consumption, other animal models should be developed that both detect IL-7 in peripheral lymphoid tissue, and can sufficiently amplify the signal from secreted IL-7 to permit visualization.

Materials and Methods

Mice

C57BL/6 mice were purchased from the Animal Production Area, NCI-FCRDC (Frederick, MD). $Rag2^{-/-}$ were originally purchased from The Jackson Laboratory (Bar Harbor, MN, USA) and maintained by homozygous breeding at NCI-Frederick, MD. Three strains of IL-7-promoter-ECFP (IL7promECFP) mice have been produced at NCI, Frederick MD and homozygous strains have been selected and maintained at NCI-Frederick, MD.

Transgenic mice expressing an IL-7 cDNA under the control of the human keratin 14 (K14) [46] promoter were maintained in specific pathogen free (SPF) conditions at the animal facility of the Department of Dermatology, Brigham and Women's Hospital, Boston, MA. Tissues from these animals were removed and processed for histopathology or RNA extraction promptly after euthanasia and shipped overnight on dry packs or dry ice to our facilities.

OT-1xRAG$^{-/-}$ (C57BL/6-*Tg(OT-I)-RAG1^{tm1Mom}*) [47] mice were purchased from Taconic Farms (Germantown, NY, USA) and maintained by homozygous breeding at NCI-Frederick, MD.

NCI-Frederick is accredited by AAALAC International and follows the Public Health Service Policy for the Care and Use of Laboratory Animals. Animal care was provided in accordance with the procedures outlined in the Guide for Care and Use of Laboratory Animals (National Research Council; 1996; National Academy Press; Washington, D.C.).

Il7 in situ hybridization

In situ hybridization (ISH) assays were developed that were specific for murine *Il7* and glyceraldehyde-3-phosphate dehydrogenase (*Gapdh*) and used to define temporal and special expression patterns in optimally processed adult mouse thymus and lymph node tissue. Sequence verified riboprobe generation templates corresponding to bps 884–1238 of *Gapdh* (Accession # NM_001001303) and bps 294–705, 792–1185 and 294–1185 of *Il7* (Acc # NM_008371) were produced via a PCR based strategy that utilized forward primers flanked by the T3 promoter and reverse primers flanked by the T7 promoter. Corresponding riboprobe pairs (sense and antisense) were then synthesized (Megascript high yield in vitro transcription kit, Ambion), purified (MEGAClear purification kit, Ambion), resuspended at 100 ng/µl in RNA storage solution (Ambion) and held at −80°C until use. Probe size and integrity have subsequently been confirmed via Agilent Bioanalyzer 2100 NanoChip analyses (data not shown). Due to anticipated very low level expression of *Il7* mRNA, HEK293 human cell line transfected with a high-level *Il7* mRNA expression construct (pECFP-N1/IL-7 or pEYFP-N1/IL-7) were prepared. Untransfected cells, transfected cells and mouse thymi and lymph nodes were harvested and fixed for 24 hrs at 4°C in freshly prepared 4% paraformaldehyde (PFA) in PBS then processed into paraffin blocks. Additional fixed tissue was cryoprotected in 20% sucrose at 4°C for 24 hrs and then embedded in OCT to generate frozen tissue blocks. Ten micron paraffin or frozen sections were then placed onto Super-Frost Plus glass microscope slides (Fisher

Scientific) and held at −20°C until ISH. Specificity of each probe was verified in a series of pilot ISH (method described in detail below) on paraffin sections of the transfected and untransfected HEK293 cells (data not shown). Within this, previous work had indicated that *Gapdh* mRNA is readily detected in HEK293 cells by chromogenic in situ hybridization (unpublished observation). Detection of the corresponding mRNA by ISH is therefore a useful positive control that indicates successful tissue fixation, pre-treatment and in situ hybridizations.

Immediately prior to ISH, representative sections were removed from −20°C, dried at 60°C for 1 hr, de-paraffinized and re-hydrated through graded ethanols into 1X Phosphate Buffered Saline with 0.1% Tween 20 (PBST). Tissue was then permeabilized with 10 µg/ml Proteinase K (Roche) in PBST for 10 min, washed twice in PBST for 2 min, post-fixed in fresh 4% PFA for 10 min, washed twice in PBST for 2 min, acetylated in 0.1 M triethanolamine (Sigma) containing 0.25% fresh acetic anhydride (Sigma) for 30 min, and washed three times in PBST for 10 min. For frozen section ISH, frozen tissue sections were submerged in room temperature 4% PFA PBS, pH 9.5 for 1 hr, washed twice in PBS pH 7.4 for 3 min then acetylated as above. Prior to hybridization, sections were pre-hybridized at 65°C for 1.5 hrs in 250 µl of hybridization buffer (50% distilled formamide, 5X SSC, 1% SDS, 50 µg/ml yeast tRNA, 50 µg/ml heparin sodium salt) then transferred into 250 µL of hybridization buffer containing 0.5 ng/µl of probe under Cover Well™ hybridization chambers (GraceBiolabs, Bend, OR) at 65°C for 18 hrs. Unbound probe was removed by washing like slides sorted by individual probe twice in 1X SSC for 15 min at room temperature, followed by 0.5X SSC for 60 min, at 65°C, and 0.5X SSC for 5 min at room temperature. Specific hybridization was then visualized via Digoxigenin specific IHC. For IHC, hybridized slides were equilibrated in maleic acid buffer, pH 7.5 (100 mM maleic acid, 150 mM NaCl, and 0.1% Tween 20) and non-specific antibody binding was blocked for 2 hrs in maleic acid buffer containing 1% non-fat dry milk. Equilibrated slides were then incubated in a 1:4,000 dilution of sheep anti-digoxigenin $F(ab)_2$ alkaline phosphatase antibody (Roche) in blocking buffer overnight at 4°C. Unbound antibody was removed by extensive washing in maleic acid buffer for 15 min. Sections were next equilibrated in chromogenic buffer (100 mM Sodium Chloride, 100 mM Tris (Sigma, pH 9.5), 50 mM Magnesium Chloride Hexahydrate and 0.1% Tween 20) then exposed to 250 µl of chromogenic substrate (BM Purple AP Substrate, Roche) for times ranging from 1 day to one week with a daily change of substrate. Following sufficient deposition of blue/purple signal, slides were rinsed with water, counter-stained with filtered Nuclear Fast Red Stain (0.1% NFR in 5% aluminum sulfate, Kernechtrot, Germany), dehydrated through graded alcohols, cleared in xylene, and cover slipped in Permount (Fisher Scientific). A positive result is indicated by the presence of blue/purple precipitate on a pink/red background and amount of signal generated per unit of time can be used to estimate abundance of a targeted transcript. Using this approach, highly abundant transcripts (e.g. *Gapdh* in tissue or cells or *Il7* in pECFP-N1/IL-7 and pEYFP-N1/IL-7 transfected cells) are readily detected with 1 day (or less) of chromogenic exposure. Failure to detect signal after 7 days in combination with anticipated signals within technical controls is consistent with very low or absent mRNA expression and indicated by absence of blue/purple color on a pink/red background.

RNA extraction from whole thymus and real time RT-PCR

C57BL/6, $Rag2^{-/-}$ and K14 mouse thymi were harvested into RNA later (Ambion) and DNA-free total RNA was isolated using Triazol reagent (Invitrogen) via a modification to the provided protocol. Briefly, following addition of chloroform and phase separation, 50X DNase I buffer (1 M Tris, pH 7.0 and 100 mM $MgCl_2$) was added to each aqueous phase to 1X final. One µl of Ambion DNase I (2 U/µl) was then added and incubated at RT for 15 min. Following completion of the standard protocol, concentration and purity of RNA yield was established by spectrophotometry (NanoDrop, NanoDrop Technologies, Wilmington, DE, USA) and quality confirmed by capillary electrophoresis (Agilent Bioanalyzer 2100 NanoChip).

Two microgram aliquots of each total RNA stock were converted into cDNA via hex primed reverse transcription (Thermoscript RT kit, Invitrogen). Each reaction was diluted with TE to produce a cDNA stock with a final volume of 100 µl and aliquots of each stock were then analyzed for relative amounts of *Il7*, *Gapdh*, and *18 s* ribosomal RNA via Taqman Gene expression analyses (Applied Biosystems) using a Stratagene MX3000P thermocyler running MxPro software (ver 3.0). Ct values generated from each sample with the *18 s* specific probe set were used to normalize expression of the two target genes (*Il7* and *Gapdh*) using a ΔCt method with correction for variation in amplification efficiency. Normalized ratios were then used to determine the variance in target gene expression versus wild type, and the variance was then used to approximately calculate the corresponding ratio of each transcript to the other.

Cell preparation from thymus and cell sorting

Single cell suspensions were prepared from thymic tissue following published procedures [48,49]. In brief, 10 thymi from C57BL/6 mice were harvested, punched with a scalpel, transferred to a beaker and stirred in 50 ml of RPMI 1640 (Mediatech Inc., Herndon, VA, USA) at 4°C for 30 min to remove the majority of the thymocytes. The resulting fragments were then digested in a series of three incubations in 5 ml of 0.125% (w/v) collagenase D/DNase I (Roche) with 0.1% (w/v) DNase I (Roche) in RPMI-1640 followed by a single digestion in 5 ml of 0.125% collagenase/dispase (Roche) with 0.1% (w/v) DNase I in RPMI-1640. Digestions were performed at 37°C for 15 min in an oven in tubes placed on the rotisserie for gentle agitation. Cells were collected after each digestion once thymic fragments had settled, pooled and kept on ice. After washing in PBS, cells were filtered through a 100 µm mesh and counted. Before staining, cells were depleted of hematopoietic cells using MACS CD45 MicroBeads (Miltenyi Biotec, Auburn, CA, USA) and autoMACS separation columns. After enrichment, cells were labeled using different combinations of the following antibodies: APC-CD45.2 (eBioscience), PE-CD11c (clone HL3, BD Pharmingen, San Jose, CA, USA), EpCAM (clone G8.8a) followed by secondary staining with PE-Cy5-anti-Rat IgG, FITC-Ly51(clone 6C3, BD Pharmingen), MTS-15 followed by secondary staining with FITC-ant-Rat IgG, and MTS-12 (anti CD31) followed by secondary staining with PE-anti-Rat IgG. Cell sorting was performed using a MoFlow Cytometer and cells were collected in RPMI-1640, washed and resuspended in lysing solution (RNAqueous-Micro Kit, Ambion, Austin, TX, USA).

RNA extraction from sorted stromal cells and absolute quantification of *Il7* mRNA by real time RT-PCR

RNA was extracted using RNAqueous-Micro Kit (Ambion) following manufacturer's protocol. After extraction, 100 ng of RNA were retrotranscribed using Superscript III First-Strand Synthesis System (Invitrogen, Carlsbad, CA, USA) and following manufacturer's instructions.